

Chapter 2

Free-Space Optical Channel Models

2.1 Atmospheric Channel

The concentric layers around the surface of the Earth are broadly classified into two regions: homosphere and heterosphere. The homosphere covers the lower layers ranging from 0–90 km. Heterosphere lies above homosphere above 90 km. The homospheric region of atmosphere is composed of various gases, water vapors, pollutants, and other chemicals. Maximum concentrations of these particles are near the Earth surface in the troposphere that extends up to 20 km. Figure 2.1 depicts the broad classification of various layers of the atmosphere, and details of each layer with their temperature values are shown in Fig. 2.2.

The density of particles decreases with the altitude up through the ionosphere (region of upper atmosphere that extends from about 90 to 600 km and contains ionized electrons due to solar radiations). These ionized electrons form a radiation belt around the surface of the Earth. These atmospheric particles interact with all signals that propagate through the radiation belt and lead to deterioration of the received signal due to absorption and scattering. Absorption is the phenomenon where the signal energy is absorbed by the particles present in the atmosphere resulting in the loss of signal energy and gain of internal energy of the absorbing particle. In scattering, there is no loss of signal energy like in absorption, but the signal energy is redistributed (or scattered) in arbitrary directions. Both absorption and scattering are strongly dependent upon operating wavelength and will lead to decrease in received power level. These effects become more pronounced when the operating wavelength of the transmitted signal is comparable with the cross-sectional dimensions of the atmospheric particles. Figure 2.3 shows transmittance (or attenuation) effects as a function of wavelength using MODTRAN software package. The output of MODTRAN in clear weather conditions is plotted for wavelength up to 3 μm . It is clear from this figure that peaks in attenuation at specific wavelengths is due to absorption by atmospheric particles and therefore the choice

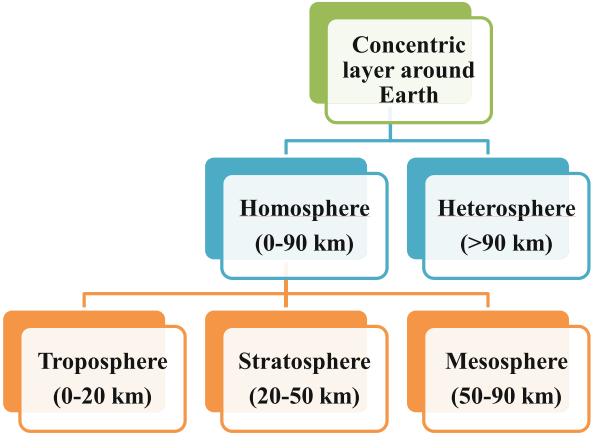


Fig. 2.1 Broad classification of atmospheric layers

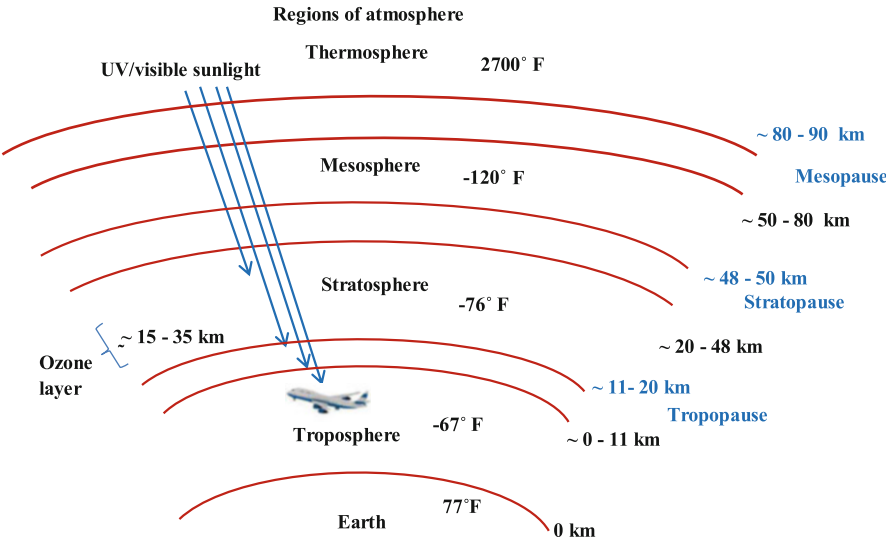


Fig. 2.2 Various atmospheric layers with corresponding temperatures

of wavelength has to be done very wisely in the high transmissive band for FSO communication links.

The atmospheric condition in FSO channel can be broadly classified into three categories, namely, clear weather, clouds, and rain. Clear weather conditions are characterized by long visibility and relatively low attenuation. Cloudy weather conditions range from mist or fog to heavy clouds and are characterized by low visibility, high humidity, and large attenuation. Rain is characterized by the presence of rain droplets of variable sizes, and it can produce severe effects depending upon rainfall rate.

Fig. 2.3 Atmospheric transmittance (attenuation) vs. wavelength [1]
(Disclaimer: This image is from a book chapter that was produced by personnel of the US Government; therefore it cannot be copyrighted and is in the public domain)

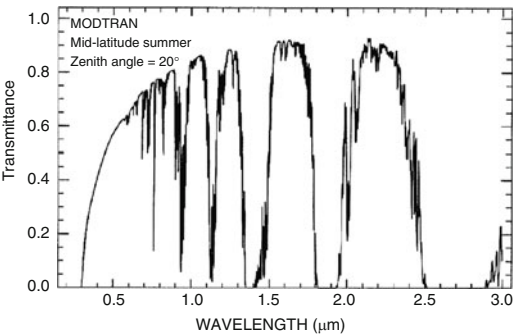
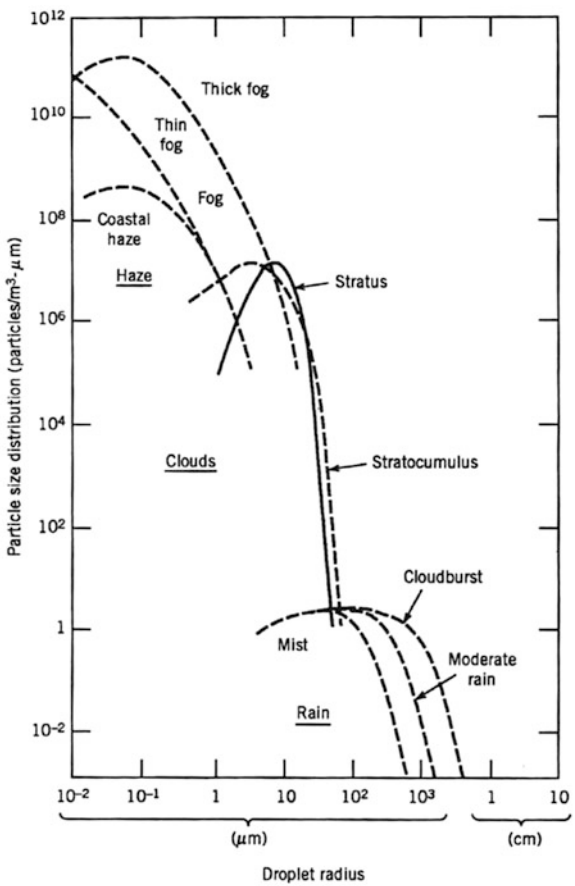


Fig. 2.4 Average particle size and corresponding particle density in atmosphere [2]



Various atmospheric conditions can be represented by size of the particle (i.e., cross-sectional dimension relative to operating wavelength) and the particle density (i.e., volumetric concentration of the particles). Figure 2.4 shows the average droplet size and its distribution for various cloudy and rainy conditions. It is seen that

conditions may vary from high density and small particle size like in the case of mist and fog to low density and large particle size during heavy rain. It should be noted that Fig. 2.4 gives average parameters, whereas real atmospheric conditions may undergo various temporal changes.

2.1.1 Atmospheric Losses

The atmospheric channel consists of various gases and other tiny particles like aerosols, dust, smoke, etc., suspended in the atmosphere. Besides these, large precipitation due to rain, haze, snow, and fog is also present in the atmosphere. Each of these atmospheric constituents results in the reduction of the power level, i.e., attenuation of optical signal due to several factors, including absorption of light by gas molecules, Rayleigh, or Mie scattering. Various types of losses encountered by the optical beam when propagating through the atmospheric optical channel are described in this section.

In FSO communication system, when the optical signal propagates through the atmosphere, it experiences power loss due to several factors as discussed in the following sections.

2.1.1.1 Absorption and Scattering Losses

The loss in the atmospheric channel is mainly due to absorption and scattering processes. At visible and IR wavelengths, the principal atmospheric absorbers are the molecules of water, carbon dioxide, and ozone [3, 4]. The attenuation experienced by the optical signal when it passes through the atmosphere can be quantified in terms of optical depth τ which correlates with power at the receiver P_R and the transmitted power P_T [5] as

$$P_R = P_T \exp(-\tau). \quad (2.1)$$

The ratio of power received to the power transmitted in the optical link is called atmospheric transmittance $T_a (= P_R/P_T)$.

When the optical signal propagates at a zenith angle θ , the transmittance factor is then given by $T_\theta = T_a \sec(\theta)$. The atmospheric transmittance T_a and the optical depth τ are related to the atmospheric attenuation coefficient γ and the transmission range R as follows:

$$T_a = \exp \left(- \int_0^R \gamma(\rho) d\rho \right) \quad (2.2)$$

and

$$\tau = \int_0^R \gamma(\rho) d\rho. \quad (2.3)$$

In both the cases, the loss in dB that the beam experiences during propagation through the atmosphere can be calculated using the following equation

$$Loss_{prop} = -10 \log_{10} T_a. \quad (2.4)$$

In the first case, this loss in dB will be 4.34τ . Hence, an optical depth of 0.7 gives a loss of 3 dB.

The attenuation coefficient is the sum of the absorption and scattering coefficients from aerosols and molecular constituents of the atmosphere and is given by [6]

$$\gamma(\lambda) = \underbrace{\alpha_m(\lambda)}_{\text{Molecular absorb. coeff.}} + \underbrace{\alpha_a(\lambda)}_{\text{Aerosol absorb. coeff.}} + \underbrace{\beta_m(\lambda)}_{\text{Molecular scatt. coeff.}} + \underbrace{\beta_a(\lambda)}_{\text{Aerosol scatt. coeff.}} \quad (2.5)$$

The first two terms in the above equation represent the molecular and aerosol absorption coefficients, respectively, while the last two terms are the molecular and aerosol scattering coefficients, respectively. The atmospheric absorption is a wavelength-dependent phenomenon. Some typical values of molecular absorption coefficients are given in Table 2.1 for clear weather conditions. The wavelength range of FSO communication system is chosen to have minimal absorption. This is referred to as atmospheric transmission windows. In this window, the attenuation due to molecular or aerosol absorption is less than 0.2 dB/km. There are several transmission windows within the range of 700–1600 nm. Majority of FSO systems are designed to operate in the windows of 780–850 and 1520–1600 nm.

The scattering process results in the angular redistribution of the optical energy with and without wavelength change. It depends upon the radius r of the particles encountered during the propagation process. If $r < \lambda$, the scattering process is classified as Rayleigh scattering; if $r \approx \lambda$, it is Mie scattering. For $r > \lambda$, the scattering process can be explained using the diffraction theory (geometric optics). The scattering process due to various scattering particles present in the atmosphere channel is summarized in Table 2.2. Out of various scattering particles like air

Table 2.1 Molecular absorption at typical wavelengths [7]

S.No	Wavelength (nm)	Molecular absorption (dB/km)
1.	550	0.13
2.	690	0.01
3.	850	0.41
4.	1550	0.01

Table 2.2 Size of various atmospheric particles present in the optical channel and type of scattering process

Type	Radius (μm)	Scattering process
Air molecules	0.0001	Rayleigh
Haze particle	0.01–1	Rayleigh-Mie
Fog droplet	1–20	Mie-Geometrical
Rain	100–10,000	Geometrical
Snow	1000–5000	Geometrical
Hail	5000–50,000	Geometrical

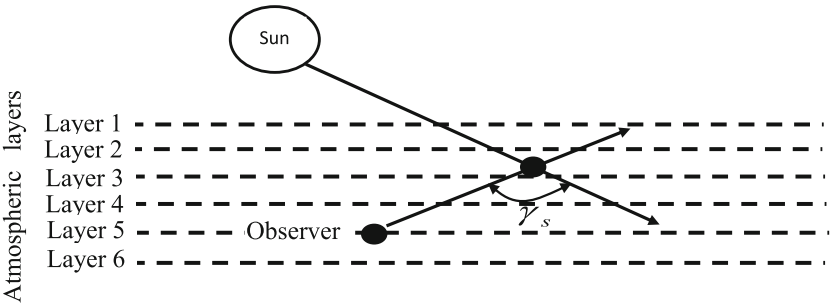


Fig. 2.5 Sky radiance due to scattering mechanism

molecules, haze particles, fog droplets, snow, rain, hail, etc., the wavelength of fog particles is comparable with the wavelength of FSO communication system. Therefore, it plays a major role in the attenuation of an optical signal.

Atmospheric scattering not only attenuates the signal beam in the atmosphere, but it is also the primary cause for sky radiance which introduces noise in daytime communication [8]. Sky radiance is due to the scattering of solar photons along the atmospheric propagating path, and it gives rise to unwanted background noise which degrades the signal-to-noise ratio at the receiver. The received background noise depends upon the geometry of the receiver and relative location of the Sun and the transmitter. Figure 2.5 shows the scattering mechanism for the layered model of the atmosphere. The atmosphere is considered to be modeled as multiple layers with each layer consisting of homogeneous mixture of gases and aerosols. The scattering angle γ_s is the angle formed between the forward direction of the Sun radiation and the point of observation. It is seen that higher the concentration of the scatterers, more will be the sky radiance. As the angular distance between the observation direction and the Sun decreases, there is an increase in sky radiance. Within 30° from the Sun, sky radiance is greatly dominated by aerosol contribution. As the angular distance from the Sun increases, the dominant source of background radiation is due to Rayleigh scattering.

2.1.1.2 Free-Space Loss

In an FSO communication system, the largest loss is usually due to “space loss,” i.e., the loss in the signal strength while propagating through free space. The space loss factor is given by

$$L_s = \left(\frac{\lambda}{4\pi R} \right)^2, \quad (2.6)$$

where R is the link range. Due to dependence on wavelength, the free-space loss incurred by an optical system is much larger (i.e., the factor L_s is much smaller) than in an RF system. Besides the space loss, there are additional propagation losses if the signal passes through a lossy medium, e.g., a planetary atmosphere. Many optical links like deep space optical links do not have additional space loss as they do not involve the atmosphere.

2.1.1.3 Beam Divergence Loss

As the optical beam propagates through the atmosphere, it spreads out due to diffraction. It may result in a situation in which the receiver aperture is not able to collect a fraction of the transmitted beam and resulting in beam divergence loss as depicted in Fig. 2.6. A typical FSO system transmits optical beam which is 5–8 cm in diameter at the transmitter. This beam spreads to roughly 1–5 m in diameters after propagating 1 km distance. However, FSO receiver has narrow field of view (FOV), and it is not capable of collecting all the transmitted power resulting in the loss of energy. Figure 2.6 depicts beam divergence loss where the receiver is capable of collecting only a small portion of the transmitted beam.

The optical power collected by the receiver is given by

$$P_R = P_T G_T G_R L_P, \quad (2.7)$$

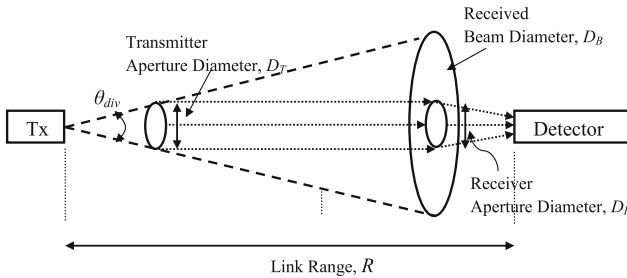


Fig. 2.6 Loss due to beam divergence

where P_T is the transmitted power, L_P the free-space path loss, and G_T and G_R the effective antenna gain of transmitter and receiver, respectively. Substituting the values of $L_P \left[= \left(\frac{\lambda}{4\pi R} \right)^2 \right]$, $G_T \left[\approx (4D_T/\lambda)^2 \right]$, and $G_R \left[\approx (\pi D_R/\lambda)^2 \right]$ (as mentioned in Chap. 1) gives received optical power as

$$P_R \approx P_T \left(\frac{D_T D_R}{\lambda R} \right)^2 \approx P_T \left(\frac{4}{\pi} \right)^2 \left(\frac{A_T A_R}{\lambda^2 R^2} \right). \quad (2.8)$$

Therefore, diffraction-limited beam divergence loss/geometric loss expressed in dB is given as

$$L_G(\text{Geometric Loss}) = -10 \left[2 \log \left(\frac{4}{\pi} \right) + \log \left(\frac{A_T A_R}{\lambda^2 R^2} \right) \right]. \quad (2.9)$$

In general, optical source with narrow beam divergence is preferable. But narrow beam divergence causes the link to fail if there is a slight misalignment between the transceivers. Therefore, an appropriate choice of beam divergence has to be made in order to eliminate the need for active tracking and pointing system and, at the same time, reduce the beam divergence loss. Many times, beam expander is used to reduce the loss due to diffraction-limited beam divergence as beam divergence is inversely proportional to the transmitted aperture diameter ($\theta_{div} \cong \lambda/D_T$). In this case, diffracting aperture is increased with the help of two converging lens as shown in Fig. 2.7.

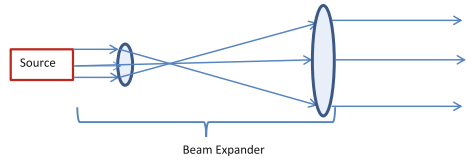
For non-diffraction-limited case, a source of divergence angle θ_{div} and diameter D_T will make the beam size of $(D_T + \theta_{div} R)$ for link distance equals to R . In this case, the fraction of received power, P_R to the transmitted power, P_T is given by

$$\frac{P_R}{P_T} = \frac{D_R^2}{(D_T + \theta_{div} R)^2}, \quad (2.10)$$

and the beam divergence or geometric loss in dB will be

$$L_G(\text{Geometric Loss}) = -20 \log \left[\frac{D_R}{(D_T + \theta_{div} R)} \right]. \quad (2.11)$$

Fig. 2.7 Beam expander to increase diffraction aperture



2.1.1.4 Loss due to Weather Conditions

The performance of FSO link is subject to various environmental factors like fog, snow, rain, etc. that leads to decrease in the received signal power. Out of these environmental factors, the atmospheric attenuation is typically dominated by fog as the particle size of fog is comparable with the wavelength of interest in FSO system. It can change the characteristics of the optical signal or can completely hinder the passage of light because of absorption, scattering, and reflection. The atmospheric visibility is the useful measure for predicting atmospheric environmental conditions. Visibility is defined as the distance that a parallel luminous beam travels through in the atmosphere until its intensity drops 2 % of its original value. In order to predict the optical attenuation statistics from the visibility statistics for estimating the availability of FSO system, the relationship between visibility and attenuation has to be known. Several models that describe the relation between visibility and optical attenuation are given in [9–11]. To characterize the attenuation of optical signal propagating through a medium, a term called “specific attenuation” is used which means attenuation per unit length expressed in dB/km and is given as

$$\beta(\lambda) = \frac{1}{R} \cdot 10 \log \left(\frac{P_0}{P_R} \right) = \frac{1}{R} 10 \log \left(e^{\gamma(\lambda)R} \right), \quad (2.12)$$

where R is the link length, P_0 the optical power emitted from the transmitter, P_R the optical power at distance R , and $\gamma(R)$ the atmospheric attenuation coefficient. The specific attenuation due to fog, snow, and rain is described below.

- (i) Effect of fog: The attenuation due to fog can be predicted by applying Mie scattering theory. However, it involves complex computations and requires detailed information of fog parameters. An alternate approach is based on visibility range information, in which the attenuation due to fog is predicted using common empirical models. The wavelength of 550 nm is usually taken as the visibility range reference wavelength. Equation (2.13) defines the specific attenuation of fog given by common empirical model for Mie scattering.

$$\beta_{fog}(\lambda) = \frac{3.91}{V} \left(\frac{\lambda}{550} \right)^{-p}, \quad (2.13)$$

where $V(\text{km})$ stands for visibility range, $\lambda(\text{nm})$ is the operating wavelength, and p the size distribution coefficient of scattering.

According to Kim model, p is given as:

$$p = \begin{cases} 1.6 & V > 50 \\ 1.3 & 6 < V < 50 \\ 0.16V + 0.34 & 1 < V < 6 \\ V - 0.5 & 0.5 < V < 1 \\ 0 & V < 0.5 \end{cases} \quad (2.14)$$

According to Kruse model, p is given as:

$$p = \begin{cases} 1.6 & V > 50 \\ 1.3 & 6 < V < 50 \\ 0.585V^{\frac{1}{3}} & V < 6 \end{cases} \quad (2.15)$$

Different weather conditions can be specified based on their visibility range values. Table 2.3 summarizes the visibility range and loss for different weather conditions.

For low visibility weather condition, that is, during heavy fog and cloud, operating wavelength has a negligible effect on the specific attenuation, whereas for light fog and haze when the visibility range is high (6 km), attenuation is quiet less for 1550 nm as compared to 850 and 950 nm. As visibility further increases beyond 20 km (clear weather), dependance of the attenuation on wavelength again decreases. This has been shown in Fig. 2.8a, b obtained by numerical simulation.

- (ii) Effect of snow: Attenuation due to snow can vary depending upon the snowflake size and snowfall rate. Since snowflakes are larger in size than raindrop, they produce deeper fades in the signal as compared to the raindrops. Snowflake size can be as large as 20 mm which can completely block the path of the optical signal depending upon the beam width of the signal. For snow,

Table 2.3 Visibility range values corresponding to weather conditions [12]

Weather condition	Visibility range (km)	Loss (dB/km) at 785 nm
Thick fog	0.2	−89.6
Moderate fog	0.5	−34
Light fog	0.770 to 1	−20 to −14
Thin fog/heavy rain (25 mm/hr)	1.9 to 2	−7.1 to −6.7
Haze/medium rain (12.5 mm/hr)	2.8 to 4	−4.6 to −3
Light haze/light rain (2.5 mm/hr)	5.9 to 10	−1.8 to −1.1
Clear/drizzle (0.25 mm/hr)	18 to 20	−0.6 to 0.53
Very clear	23 to 50	−0.46 to −0.21

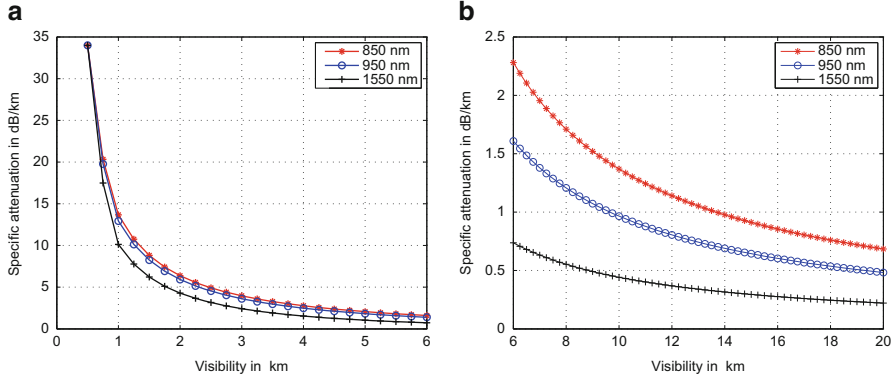


Fig. 2.8 Attenuation vs. visibility. (a) For heavy fog and cloud. (b) For light fog and haze

attenuation can be classified into dry and wet snow attenuation. The specific attenuation (dB/km) for snow rate S in mm/hr is given by following equation

$$\beta_{snow} = aS^b, \quad (2.16)$$

where the values of parameters a and b in dry and wet snow are

$$\text{Dry snow : } a = 5.42 \times 10^{-5} + 5.4958776, \quad b = 1.38 \quad (2.17)$$

$$\text{Wet snow: } a = 1.023 \times 10^{-4} + 3.7855466, \quad b = 0.72 .$$

The snow attenuation based on visibility range can be approximated by the following empirical model

$$\alpha_{snow} = \frac{58}{V} \quad (2.18)$$

- (iii) Effect of rain: The sizable rain droplets can cause wavelength-independent scattering, and the attenuation produced by rainfall increases linearly with rainfall rate. The specific attenuation for rain rate R (mm/hr) is given by

$$\beta_{rain} = 1.076R^{0.67} \quad (2.19)$$

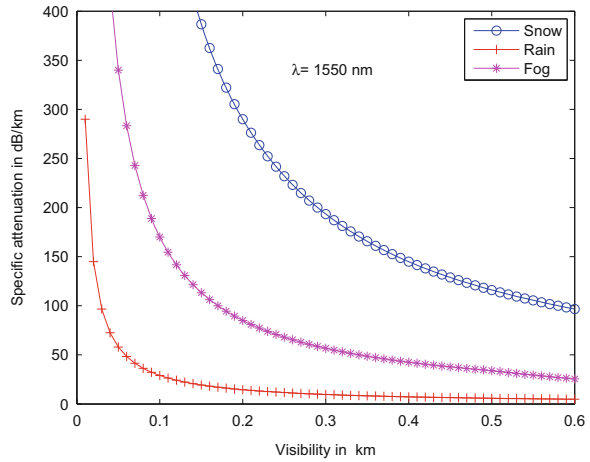
The rain attenuation for FSO links can be reasonably well approximated by empirical formula and is given by

$$\alpha_{rain} = \frac{2.8}{V} \quad (2.20)$$

where V is visibility range in km and its values based on rainfall rate is summarized in Table 2.4.

Table 2.4 Rainfall rates and their visibility ranges [13]

Rainfall type	Rainfall rate, R (mm/hr)	Visibility range, V (km)
Heavy rain	25	1.9–2
Medium rain	12.5	2.8–40
Light rain/drizzle	0.25	18–20

Fig. 2.9 Attenuation for fog, snow and rain

It is clear from Fig. 2.9 that the attenuation is maximum for snow and lesser for rain as compared to fog. In case of fog, there is a sudden increase in attenuation for visibility range less than 150 m. Visibility range <150 m corresponds to heavy fog and cloudy weather.

2.1.1.5 Pointing Loss

The loss that occurs due to imperfect alignment between transmitter and receiver is called pointing loss. A large pointing loss can lead to intolerable signal fades and can significantly degrade the system performance. It is due to the fact that the random platform jitter is generally much larger than the transmitter beam width. Hence, a very tight acquisition, tracking, and pointing (ATP) subsystem is required to reduce the loss due to misalignment. The transmitted power that is allocated for the pointing of the optical beam is not used for communication. Therefore, it is highly desirable to keep the pointing loss due to misalignment of the narrow laser beam as small as possible so that the sufficient power is available for communication. It is desirable to achieve sub-microradian pointing system by using inertial sensors, focal plane arrays, and the steering mirror. The pointing loss of the transmitter that must be considered for the link budget analysis is given as

$$L_p = \exp\left(\frac{-8\theta_{jitter}^2}{\theta_{div}^2}\right), \quad (2.21)$$

where θ_{jitter} is the beam jitter angle and θ_{div} the transmitter beam divergence as shown in Fig. 2.6.

2.1.2 Atmospheric Turbulence

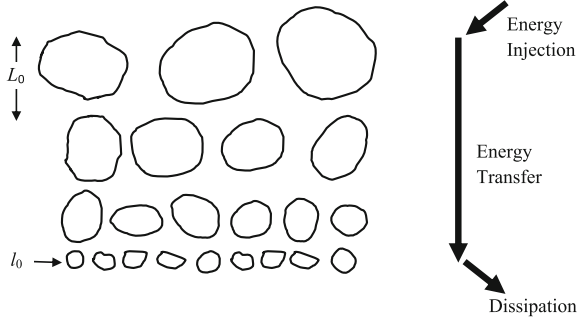
The atmosphere can be thought as a viscous fluid that has two distinct states of motion, i.e., laminar and turbulent. In laminar flow, the velocity flow characteristics are uniform, or they change in some regular fashion. In case of turbulent flow, the velocity loses its uniform characteristics due to dynamic mixing and acquire random sub-flows called turbulent eddies. The transition from laminar to turbulent motion is determined by the nondimensional quantity called Reynolds number. This number is defined as $Re = \mathbf{V}l_f/\nu_k$, where \mathbf{V} is the characteristic velocity (in m/s), l_f the dimension of flow (in m), and ν_k the kinematic viscosity (in m^2/s). If the Reynolds number exceeds the “critical Reynolds Number,” the flow is considered turbulent in nature. Near the ground, the characteristic scale size l_f is approximately 2 m, wind velocity is 1 to 5 m/s, and ν_k is about $0.15 \times 10^{-4} m^2/s$. This gives a large value for the Reynolds number of the order of $Re \sim 10^5$. Therefore, close to the ground level, the flow may be considered to be highly turbulent.

In order to understand the structure of atmospheric turbulence, it is convenient to adopt the energy cascade theory of turbulence [14, 15]. As per this theory, when the wind velocity is increased, the Reynolds number exceeds the critical value. This results in the local unstable air masses called turbulent eddies with their characteristic dimensions slightly smaller than, and independent of, the parent flow [16]. Under the influence of the inertial forces, the larger size eddies break up into smaller eddies until the inner scale size l_0 is reached. The family of eddies bounded above by the outer scale L_0 and below by the inner scale l_0 forms the inertial subrange. The outer scale denotes the scale below which the turbulent properties are independent of the parent flow. Typically, the outer scale is in the order of about 10 to 100 m and is usually assumed to grow linearly with the height above the ground. The inner scale is of the order of 1 to 10 mm near the ground, but it is of the order of centimeters or more in the troposphere and stratosphere. Scale size smaller than the inner scale l_0 belongs to the viscous dissipation range. In this range, the turbulent eddies disappear, and the remaining energy is dissipated in the form of heat. This phenomenon is known as Kolmogorov theory [17] of turbulence and is depicted in Fig. 2.10.

The mathematical model of the atmospheric turbulence and its effects on the optical beam propagation assumes that the fluctuations in the atmospheric parameter are stationary random processes having statistically homogeneous and isotropic nature. Within this mathematical framework, the structure function in the inertial range satisfies the universal two-thirds power law, i.e., it follows $r^{2/3}$ dependence, where r refers to the spatial scale defined as

$$r = |\vec{r}_1 - \vec{r}_2|, \quad l_0 \leq r \leq L_0, \quad (2.22)$$

Fig. 2.10 Kolmogorov model where L_0 and l_0 are the outer and inner scale of turbulent eddies, respectively



where \vec{r}_1 and \vec{r}_2 refer to position vectors at two points separated by distance r in space. The structure function for a random variable $x(r)$ is then given as

$$\begin{aligned} D_x(r) &= D_x(\vec{r}_1, \vec{r}_2) \\ &= \langle |x(\vec{r}_1) - x(\vec{r}_2)|^2 \rangle. \end{aligned} \quad (2.23)$$

The random variable $x(r)$ is assumed to have a mean and a superimposed fluctuating component that is represented as

$$x(r) = \langle x(\vec{r}) \rangle + x'(\vec{r}). \quad (2.24)$$

In the above equation, the first term in the angle bracket is the slowly varying mean component and second term the random fluctuations. Using Eq. (2.24), the structure function in Eq. (2.23) can be rewritten as

$$D_x(r) = [\langle x(\vec{r}_1) \rangle - \langle x(\vec{r}_2) \rangle]^2 + \langle [x'(\vec{r}_1) - x'(\vec{r}_2)]^2 \rangle. \quad (2.25)$$

The first term in Eq. (2.25) becomes zero for a stationary random process. This makes structure function a useful parameter for describing the random fluctuations. With the atmosphere as the propagation medium, these random fluctuations can be associated with any of these parameters, i.e., velocity, temperature, and refractive index. The structure function for wind velocity $D_v(r)$ is given as [16]

$$D_v(r) = \langle (v_1 - v_2)^2 \rangle = C_v^2 r^{2/3}, \quad l_0 \leq r \leq L_0, \quad (2.26)$$

where v_1 and v_2 are the velocity components at two points separated by distance r and C_v^2 the velocity structure constant (in $\text{m}^4/3/\text{s}^2$) that measures the amount of energy in the turbulence. Similarly, the structure function for the temperature is given as $D_t(r) = C_t^2 r^{2/3}$, where C_t^2 is the temperature structure constant (in $\text{deg}^2/\text{m}^2/3$). The turbulence in the atmosphere also results from the random fluctuations of the atmospheric refractive index n due to variations in temperature

and pressure along the propagation path in the atmosphere. In general, the refractive index of the atmosphere at any point r in space can be expressed as sum of the average and the fluctuating terms, i.e.,

$$n(r) = n_0 + n'(r), \quad (2.27)$$

where $n_0 = \langle n(r) \rangle \approx 1$ is the mean value of index of refraction and $n'(r)$ represents the random deviation of $n(r)$ from its mean value. Therefore, the above equation can be rewritten as

$$n(r) = 1 + n'(r). \quad (2.28)$$

The index of refraction of the atmosphere is related to temperature and pressure of the atmosphere and is given as

$$\begin{aligned} n(r) &= 1 + 7.66 \times 10^{-6} \left(1 + 7.52 \times 10^{-3} \lambda^{-2} \right) \frac{P'(r)}{T'(r)} \\ &\cong 1 + 79 \times 10^{-6} \left(\frac{P'(r)}{T'(r)} \right), \end{aligned} \quad (2.29)$$

where λ is the wavelength in μm , P' the atmospheric pressure in mbar, and T' the temperature of the atmosphere in Kelvin. Changes in the optical signal due to absorption or scattering by the molecules or aerosols are not considered here. The structure function for refractive index, $D_n(r)$, can be expressed as $D_n(r) = C_n^2 r^{2/3}$, where C_n^2 is called refractive index structure constant [16] and is a measure of the strength of fluctuations in the refractive index. C_n^2 is related to temperature structure constant, C_t^2 as

$$C_n^2 = \left[79 \times 10^{-6} \frac{P'}{T'^2} \right]^2 C_t^2. \quad (2.30)$$

The C_t^2 is determined by taking the measurements of mean square temperature between two points separated by a certain distance along the propagation path (in $\text{deg}^2/\text{m}^{2/3}$). The other parameters are as defined earlier. It is obvious from Eq. (2.30) that refractive index structure parameter can be obtained by measuring temperature, pressure, and temperature spatial fluctuations along the propagation path. All the expressions for the structure function are defined for the inertial subrange, i.e., for $l_0 \ll r \ll L_0$. Out of all the structure constants referred above, the refractive index structure constant, i.e., C_n^2 , is considered the most critical parameter along the propagation path in characterizing the effects of atmospheric turbulence.

Depending on the size of turbulent eddy and transmitter beam size, three types of atmospheric turbulence effects are observed:

- **Beam Wander (or beam steering):** If the size of eddies are larger than the transmitter beam size, it will deflect the beam as a whole in random manner from its original path. This phenomenon is called beam wander, and it effectively leads to pointing error displacement of the beam that causes the beam to miss the receiver.
- **Beam Scintillation:** If the eddy size is of the order of beam size, then the eddies will act like lens that will focus and de-focus the incoming beam leading to irradiance fluctuations at the receiver and the process is called scintillation. Scintillations cause the loss of signal-to-noise ratio and result in deep random signal fades. The effect of scintillation can be reduced by employing techniques like multiple transmit/receive antennae, aperture averaging, etc.
- **Beam Spreading:** If the eddy size is smaller than the beam size, then a small portion of the beam will be diffracted and scattered independently. This will lead to reduction in the received power density and will also distort the received wavefront. However, the effect of turbulence-induced beam spreading will be negligible if the transmitter beam diameter is kept smaller than the coherence length of the atmosphere [18] or if the receiver aperture diameter is kept greater than the size of first Fresnel zone $\sqrt{R/k}$ [19]. In this case, the only effect will be due to turbulence-induced beam wander effect and scintillation effect.

2.1.2.1 The Effect of Beam Wander

Beam wander is the random deflection of the optical beam as it propagates through the large-scale inhomogeneities present in the turbulent atmosphere. In case of FSO uplink communication from ground to satellite, when the target is in the far field and turbulence exists in the near field of the transmitter, beam diameter is often smaller than the outer scale of the turbulence. In this case, the Gaussian profile of an optical beam gets highly skewed over short duration after propagating through turbulent atmosphere. In this process, the instantaneous point of maximum irradiance, known as “hot spot,” gets displaced from its on-axis position. The movement of hot spot and short-term beam centroid will effectively lead to outer large circle over a long period of time and is called as long-term spot size. The long-term spot size is the result of beam wander, free-space diffraction spreading, and additional spreading due to small-scale turbulent eddies smaller than beam size. The long-term spot size is therefore given as [20–22]

$$W_{LT}^2(R) = \underbrace{W^2(R) + W^2(R)T_{ss}}_{\text{Beam Spread, } W_{ST}^2} + \underbrace{\langle r_c^2 \rangle}_{\text{Beam Wander}}, \quad (2.31)$$

where $W(R)$ is the beam size after propagating distance R and T_{ss} describes the short-term spread of the beam due to atmospheric turbulence. The combined movement of the hot spot and short-term beam as depicted in Fig. 2.11a leads to the large outer circle over a long time period, and it is called long-term spot size W_{LT} as

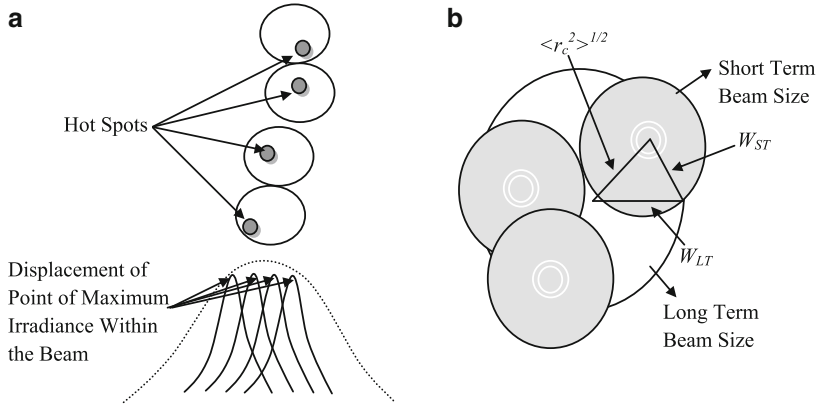


Fig. 2.11 Beam wander effect described by (a) Movement of the “hot spot” within the beam and (b) Beam wander variance $\langle r_c^2 \rangle^{1/2} = \sqrt{W_{LT}^2 - W_{ST}^2}$, where W_{ST} is the short-term beam radius and W_{LT} the long-term beam radius at the receiver (the shaded circles depict random motion of the short-term beam in the receiver plane [16])

shown in Fig. 2.11b. Therefore, the resultant long-term spot size is the superposition of the instantaneous spots that reach the receiver. The first term in Eq. (2.31) is due to free-space diffraction, middle term the additional spreading by the turbulent eddies of size smaller than the beam size, and last term the beam wander displacement variance caused by the large-size turbulent eddies. By making use of appropriate filters that only permit random inhomogeneities of size equal to or greater than beam size, the effect due to small-scale spread will be eliminated, and only contribution will be due to beam wander effect. *It should be noted that beam wander effect is negligible in case of downlink signals from the satellites.* This is because the beam size when reaches the atmosphere is much larger than the turbulent eddy size and that would not displace the beam centroid significantly. Instead, the wavefront tilt at the receiver produced by the atmospheric turbulence gives rise to angle of arrival fluctuations. The beam wander displacement variance $\langle r_c^2 \rangle$ for a collimated uplink beam is given as [22]

$$\langle r_c^2 \rangle = 7.25 (H - h_0)^2 \sec^3(\theta) W_0^{-1/3} \int_{h_0}^H C_n^2(h) \left(1 - \frac{h - h_0}{H - h_0}\right)^2 dh, \quad (2.32)$$

where $C_n^2(h)$ is the refractive index structure parameter, θ the zenith angle, W_0 the transmitter beam size, H and h_0 are the altitude of satellite and transmitter, respectively. For ground-based transmitter, $h_0 = 0$, and satellite altitude $H = h_0 + R \cos(\theta)$. Equation (2.32) can now be rewritten as [22]

$$\langle r_c^2 \rangle \approx 0.54 (H - h_0)^2 \sec^2(\theta) \left(\frac{\lambda}{2W_0}\right)^2 \left(\frac{2W_0}{r_0}\right)^{5/3}, \quad (2.33)$$

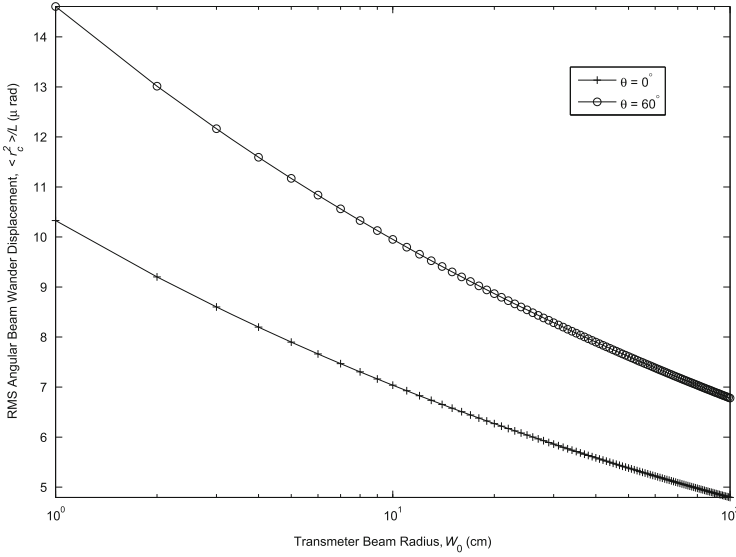


Fig. 2.12 The rms angular beam wander variance as a function of transmitter beam radius for ground-to-satellite FSO link

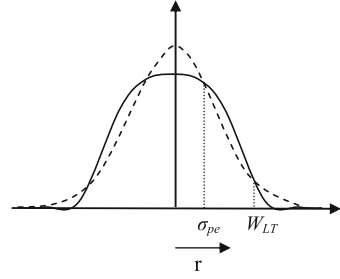
where r_0 is the atmospheric coherence length (i.e., Fried parameter) and is given as

$$r_0 = \begin{cases} (1.46C_n^2 k^2 R)^{-3/5} & \text{for horizontal link} \\ \left[0.423k^2 \sec(\theta) \int_{h_0}^H C_n^2(h) dh \right]^{-3/5} & \text{for vertical link.} \end{cases} \quad (2.34)$$

It is seen from Eqs. (2.33) and (2.34) that beam wander variance involves the free-space diffraction angle $(\lambda/2W_0)$ and tilt phase fluctuations averaged over the transmitter aperture and is of the order of $(2W_0/r_0)^{5/3}$. Variations of $\langle r_c^2 \rangle$ with W_0 for zenith angles ($\theta = 0^\circ$ and 60°) and $R = 40,000$ km are shown in Fig. 2.12. It is seen from this figure that the angular beam wander displacement variance is large for small beam size W_0 and decreases rapidly with the increase in the value of W_0 .

The beam wander effect causes widening of the long-term beam profile near the boresight that flattens the top of the beam as shown in Fig. 2.13. The flattened beam profile effectively leads to effective pointing error of the beam σ_{pe} , and this results in the increase of scintillation index σ_I^2 , discussed in the next section. In other words, the turbulence-induced beam wander effect effectively leads to pointing error displacement that can significantly affect the channel.

Fig. 2.13 Flattened beam profile as a function of radial displacement that leads to effective pointing error σ_{pe}



2.1.2.2 The Scintillation Effect

The irradiance fluctuations within the cross section of the received beam after propagating through turbulent atmosphere are commonly referred as “scintillation” and are measured in terms of scintillation index (or normalized variance of irradiance) σ_I^2 . It causes loss of signal-to-noise ratio and induces deep signal fades. The σ_I^2 is defined as [23]

$$\sigma_I^2 = \frac{\langle I^2 \rangle - \langle I \rangle^2}{\langle I \rangle^2} = \frac{\langle I^2 \rangle}{\langle I \rangle^2} - 1, \quad (2.35)$$

where I is the irradiance (intensity) at some point in the detector plane and the angle bracket $\langle \rangle$ denotes an ensemble average. For X amplitude of the transmitted optical beam, the received irradiance, I , at the receiver takes the form as

$$I = I_0 \exp [2X - 2E[X]], \quad (2.36)$$

where I_0 is the intensity without turbulence. From Eqs. (2.35) and (2.36), σ_I^2 in terms of log-amplitude variance, σ_x^2 is given by

$$\sigma_I^2 \approx 4\sigma_x^2, \text{ for } \sigma_x^2 \ll 1. \quad (2.37)$$

Further, the variance of log irradiance (also called Rytov variance) σ_R^2 is related to σ_I^2 as below

$$\sigma_I^2 = \exp(\sigma_R^2) - 1 \approx \sigma_R^2 \text{ for } \sigma_R^2 \ll 1. \quad (2.38)$$

In weak turbulence, scintillation index is expressed as

$$\sigma_I^2 = \sigma_R^2 = 1.23 C_n^2 k^{7/6} R^{11/6} \text{ for plane waves} \quad (2.39)$$

and

$$\sigma_I^2 = 0.4\sigma_R^2 = 0.5 C_n^2 k^{7/6} R^{11/6} \text{ for spherical waves, respectively,} \quad (2.40)$$

where k is wave number ($=2\pi/\lambda$). It is clear from Eqs. (2.39) and (2.40) that for a weak turbulence conditions, longer wavelength will experience lesser irradiance fluctuations for a given link range. Scintillation index for strong turbulence is given by

$$\sigma_I^2 = \begin{cases} 1 + \frac{0.86}{\sigma_R^{4/5}}, \sigma_R^2 \gg 1 & \text{for plane wave} \\ 1 + \frac{2.73}{\sigma_R^{4/5}}, \sigma_R^2 \gg 1 & \text{for spherical wave} \end{cases} \quad (2.41)$$

Clearly, Eq. (2.41) shows that for strong turbulence, smaller wavelength will experience lesser irradiance fluctuations.

Various studies have been performed to develop the mathematical model for the probability density function (PDF) of the randomly fading received signal irradiance. These studies have led to various statistical models that can describe the turbulence-induced scintillation over a wide range of atmospheric conditions.

For weak turbulence, $\sigma_I^2 < 1$, and the irradiance statistics is given by lognormal model. This model is widely used due to its simplicity in terms of mathematical computations. The PDF of the received irradiance, I , is given as

$$f(I) = \frac{1}{\sqrt{2\pi\sigma_I^2 I}} \exp \left[-\frac{(\ln(I) - \mu)^2}{2\sigma_I^2} \right], \quad (2.42)$$

where μ is the mean of $\ln(I)$. Since $\sigma_I^2 = 4\sigma_x^2$, the above lognormal pdf can be rewritten as

$$f(I) = \frac{1}{2\sqrt{2\pi\sigma_x^2 I}} \exp \left[-\frac{(\ln(I) - \mu)^2}{8\sigma_x^2} \right]. \quad (2.43)$$

When the strength of turbulence increases, lognormal pdf shows large deviation as compared to experimental data. Therefore, lognormal statistics is not appropriate model in case of strong fluctuation regimes.

For strong turbulence, $\sigma_I^2 \geq 1$, and the field amplitude is Rayleigh distributed which in turn leads to negative exponential statistics for received irradiance [2]. Its pdf is given by

$$f(I) = \frac{1}{I_0} \exp \left(-\frac{I}{I_0} \right), \quad I \geq 0, \quad (2.44)$$

where I_0 is the mean irradiance. In this case, $\sigma_I^2 \approx 1$, and this happens only far into saturation regime.

Besides these two models, a number of other statistical models [24] are there in the literature to describe the scintillation statistics in either a regime of strong turbulence (K model) or all the regimes (I - K and gamma-gamma [25] models). For $3 < \sigma_I^2 < 4$, the intensity statistics is given by K distribution. Thus K distribution describes only the strong turbulence intensity statistics. This model was originally proposed for non-Rayleigh sea echo, but later it was discovered that it is an appropriate model for characterizing the amplitude fluctuations in strong atmospheric conditions. Its pdf is given by

$$f(I) = \frac{2}{\Gamma(\alpha)} \alpha^{\frac{\alpha+1}{2}} I^{\frac{\alpha-1}{2}} K_{\alpha-1}(2\sqrt{\alpha}I), \quad I > 0, \quad (2.45)$$

where α is a channel parameter related to the effective number of discrete scatterers and $\Gamma(\cdot)$ is the well-known gamma function. When $\alpha \rightarrow \infty$, the gamma distribution function approaches delta function, and K distribution reduces to negative exponential distribution. However, K distribution lacked the numerical computation in closed form. Also, it cannot easily relate the mathematical parameters with the observables of atmospheric turbulence, and therefore, it limits the applicability and utilization.

Another generalized form of K distribution that is applicable to all conditions of atmospheric turbulence, including weak turbulence for which the K distribution is not theoretically applicable, is I - K distribution. In this case, the field of optical wave is modeled as sum of coherent (deterministic) component and a random component. The intensity is assumed to be governed by the generalized Nakagami distribution. The pdf of I - K distribution is given by [26]

$$f(I) = \begin{cases} 2\alpha(1+\rho)\left(1+\frac{1}{\rho}\right)^{\frac{\alpha-1}{2}} I^{\frac{\alpha-1}{2}} K_{\alpha-1}(2\sqrt{\alpha\rho}) I_{\alpha-1}(2\sqrt{\alpha(1+\rho)I}), & 0 < I < \frac{\rho}{1+\rho} \\ 2\alpha(1+\rho)\left(1+\frac{1}{\rho}\right)^{\frac{\alpha-1}{2}} I^{\frac{\alpha-1}{2}} I_{\alpha-1}(2\sqrt{\alpha\rho}) K_{\alpha-1}(2\sqrt{\alpha(1+\rho)I}), & I > \frac{\rho}{1+\rho} \end{cases}, \quad (2.46)$$

where $I_a(\cdot)$ is the modified Bessel function of first kind of order a . The normalized I - K distribution in the above equation involves two empirical parameters ρ and α whose values are selected by matching the first three normalized moments of the distribution. The parameter ρ is a measure of the power ratio of mean intensities of the coherent and random components of the field. The value of ρ is relatively large for extremely weak turbulence. By properly selecting the values of α and ρ , both weak and strong turbulence can be obtained. Because of the symmetry of the functional forms involving the I and K Bessel functions, this distribution is henceforth referred to as the I - K distribution. The I - K distribution reduces to the K distribution in the limit $\rho \rightarrow 0$.

However, I - K distribution is difficult to express in closed-form expressions. In that case, the gamma-gamma distribution is used to successfully describe the scintillation statistics for weak to strong turbulence. In this model, the normalized irradiance, I , is defined as the product of two independent random variables, i.e., $I = I_X I_Y$, where I_X and I_Y represent large-scale and small-scale turbulent eddies

and each of them following a gamma distribution. This leads to gamma-gamma distribution whose pdf is given as

$$f_I(I) = \frac{2(\alpha\beta)^{(\alpha+\beta)/2}}{\Gamma(\alpha)\Gamma(\beta)} I^{((\alpha+\beta)/2)-1} K_{\alpha-\beta}\left(2\sqrt{\alpha\beta}I\right), \quad I > 0, \quad (2.47)$$

where $K_a(\cdot)$ is the modified Bessel function of second kind of order a . The parameters α and β are the effective number of small-scale and large-scale eddies of the scattering environment and are related to the atmospheric conditions through the following expressions

$$\alpha = \left[\exp \left[\frac{0.49\chi^2}{(1 + 0.18d^2 + 0.5\chi^{12/5})^{7/6}} \right] - 1 \right]^{-1} \quad (2.48)$$

and

$$\beta = \left[\exp \left[\frac{0.51\chi^2 (1 + 0.69\chi^{12/5})^{-5/6}}{(1 + 0.9d^2 + 0.62d^2\chi^{12/5})^{7/6}} \right] - 1 \right]^{-1} \quad (2.49)$$

where $\chi^2 = 0.5C_n^2 k^{7/6} R^{11/6}$ and $d = (kD_R^2/4R)^{1/2}$. The parameter $k = \frac{2\pi}{\lambda}$ is the optical wave number, D_R the diameter of the receiver collecting lens aperture, and R the link range in meters, C_n^2 refractive index structure parameter whose value varies from $10^{-13} \text{ m}^{-2/3}$ for strong turbulence to $10^{-17} \text{ m}^{-2/3}$ for weak turbulence. Since the mean value of this turbulence model is $E[I] = 1$ and the second moment is given by $E[I^2] = (1 + 1/\alpha)(1 + 1/\beta)$, therefore, scintillation index (SI), that gives the strength of atmospheric fading, is defined as

$$SI = \frac{E[I^2]}{(E[I])^2} - 1 = \frac{1}{\alpha} + \frac{1}{\beta} + \frac{1}{\alpha\beta}. \quad (2.50)$$

While still mathematically complex, the gamma-gamma distribution can be expressed in closed form and can relate to various values of scintillation index unlike I - K distribution [2]. Figure 2.14 shows the range of scintillation index for various types of distribution used to model the intensity statistics.

Another turbulence model proposed in [27] is double generalized gamma (double GG) distribution which is suitable for all regimes of turbulence, and it covers almost all the existing statistical models of irradiance fluctuations as special cases.

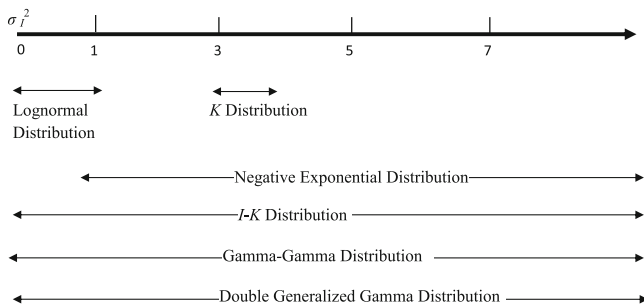


Fig. 2.14 Various distributions for intensity statistics

2.1.3 Effect of Atmospheric Turbulence on Gaussian Beam

Let us consider a Gaussian beam with amplitude A_0 propagating in free space and the transmitter located at $z = 0$. The amplitude distribution in this plane is a Gaussian function with effective beam radius W_0 defined as the radius at which the field intensity falls off to $1/e$ of that on the beam axis. The Gaussian beam at $z = 0$ is described by

$$U_0(r, 0) = A_0 \exp\left(-\frac{r^2}{W_0^2} - i\frac{kr^2}{2F_0}\right), \quad (2.51)$$

where r is the distance from beam center line in the transverse direction, k ($= 2\pi/\lambda$) the optical wave number as defined earlier, and F_0 the phase front radius of curvature which specifies the beam forming. The cases $F_0 > 0$, $F_0 = \infty$, and $F_0 < 0$ correspond to converging, collimated, and diverging beam forms, respectively, [28] as shown in Fig. 2.15.

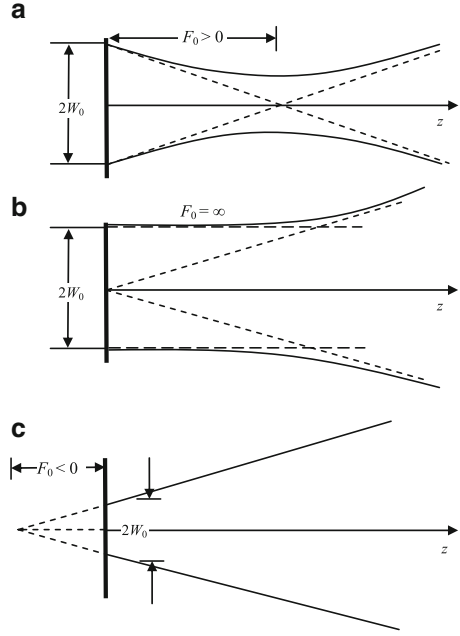
For a propagation path of range R along positive z axis, the free-space Gaussian beam wave is described as [22]

$$U_0(r, R) = \frac{A_0}{\Theta_0 + i\Lambda_0} \exp\left(ikR - \frac{r^2}{W^2} - i\frac{kr^2}{2F'}\right). \quad (2.52)$$

The parameters Θ_0 and Λ_0 are referred to as transmitter beam parameters as they are defined in terms of beam characteristics at the transmitter and are given as

$$\Theta_0 = 1 - \frac{R}{F_0}, \quad \Lambda_0 = \frac{2R}{kW_0^2}. \quad (2.53)$$

Fig. 2.15 Representation of (a) convergent beam, (b) collimated beam, and (c) divergent beam, respectively



The parameter Θ_0 represents the amplitude change in the wave due to focusing (refraction) and Λ_0 the amplitude change due to diffraction. The parameter Θ_0 is also called curvature parameter and Λ_0 the Fresnel ratio at the transmitter plane. The other parameters W and in Eq. (2.52) are the effective beam radius and phase front radius of curvature of the beam, respectively, at the receiver plane. With transmitter beam parameters as described above, the receiver beam parameters are given by

$$\Theta = 1 + \frac{R}{F'} = \frac{\Theta_0}{\Theta_0^2 + \Lambda_0^2}, \quad (2.54)$$

$$\Lambda = \frac{2R}{kW^2} = \frac{\Lambda_0}{\Theta_0^2 + \Lambda_0^2}. \quad (2.55)$$

Like their counterparts, Θ_0 and Λ_0 , the receiver parameter Θ describes the focusing or refractive effect on the amplitude of the wave and Λ the diffraction effects on the amplitude (i.e., diffractive spreading of the wave). The parameters W and F' are related to beam parameters as [22]

$$W = W_0 (\Theta_0 + \Lambda_0)^{1/2} = \frac{W_0}{(\Theta^2 + \Lambda^2)^{1/2}}, \quad (2.56)$$

$$F' = \frac{F_0 (\Theta^2 + \Lambda^2 - \Theta)}{(\Theta - 1)(\Theta^2 + \Lambda^2)} = \frac{F_0 (\Theta_0^2 + \Lambda_0^2) (\Theta_0 - 1)}{\Theta_0^2 + \Lambda_0^2 - \Theta_0}. \quad (2.57)$$

The free-space irradiance profile (without atmospheric turbulence) at the receiver plane is the square magnitude of the field given in Eq. (2.52) and is given as

$$I_0(r, R) = |U_0(r, R)|^2. \quad (2.58)$$

From Eqs. (2.52) and (2.58), we get

$$I_0(r, R) = \left(\frac{A_0^2}{\Theta_0^2 + \Lambda_0^2} \right) \exp\left(-\frac{2r^2}{W^2}\right) \quad (\text{W/m}^2). \quad (2.59)$$

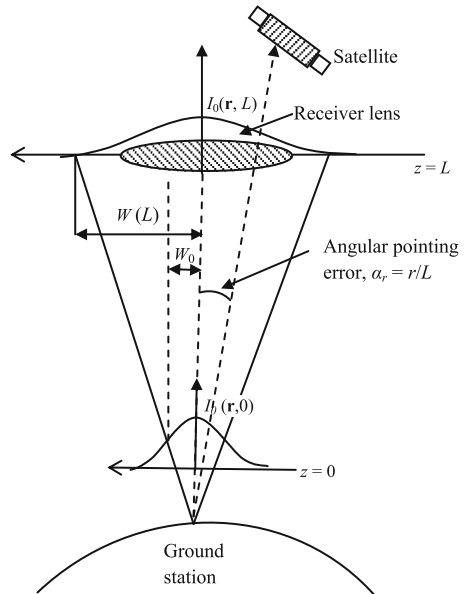
Since $\sqrt{\Theta^2 + \Lambda^2} = 1/\sqrt{\Theta_0^2 + \Lambda_0^2}$, the above equation can be written as

$$I_0(r, R) = A_0^2 (\Theta^2 + \Lambda^2) \exp\left(-\frac{2r^2}{W^2}\right). \quad (2.60)$$

The on-axis irradiance is $I_0(0, R) = \left(\frac{A_0^2}{\Theta_0^2 + \Lambda_0^2} \right) = A_0^2 (\Theta^2 + \Lambda^2)$. Figure 2.16 shows the uplink Gaussian beam profile illustrating the spot size $W(R)$, mean transmit intensity $I_0(r, 0)$, mean received intensity $I_0(r, R)$, and angular pointing error α_r .

When a Gaussian beam propagates through the turbulent atmosphere, it experiences various deleterious effects including beam spreading, beam wander, and beam scintillation that will result in variation of Gaussian beam parameters. For weak atmospheric fluctuations, the solution of wave equation for various propagation problems can be analyzed by conventional Rytov approximation. However, this

Fig. 2.16 Gaussian beam profile parameters for uplink propagation path



approximation is limited to weak fluctuation conditions as it does not account for decreasing transverse spatial coherence radius of the propagating wave. Therefore, a relatively simple model for irradiance fluctuations for Gaussian beam wave that is applicable in weak to strong turbulence has been suggested by modifying the conventional Rytov approximation. The modified Rytov approximation can be used to describe the irradiance fluctuations throughout the propagation path near the ground and allows us to extend the weak fluctuation results to moderate/strong fluctuation regime. In the following subsections, the Gaussian beam propagation using conventional Rytov approximation is discussed, and then the discussion is extended to modified Rytov approximation.

2.1.3.1 Conventional Rytov Approximation

In the conventional Rytov approximation, it is assumed that the optical field at link range R from the transmitter is given by

$$\begin{aligned} U(r, R) &= U_0(r, R) \exp[\Psi(r, R)] \\ &= U_0(r, R) \exp[\Psi_1(r, R) + \Psi_2(r, R) + \dots], \end{aligned} \quad (2.61)$$

where $U_0(r, R)$ is the free-space diffraction-limited Gaussian beam wave at the receiver given by Eq. (2.52) and $\Psi(r, R)$ the complex phase fluctuations of the field due to random refractive index inhomogeneities along the propagation path R . The parameters $\Psi_1(r, R)$ and $\Psi_2(r, R)$ are the first-order and second-order perturbations, respectively. The statistical moments of the optical field given in Eq. (2.61) involve the ensemble average of the first- and second-order perturbations. The first-order moment is given as

$$\langle U(r, R) \rangle = U_0(r, R) \langle \exp[\Psi(r, R)] \rangle. \quad (2.62)$$

The second-order moment, also called mutual coherence function [16] (MCF), is given by

$$\begin{aligned} \Gamma_2(r_1, r_2, R) &= \langle U(r_1, R) U^*(r_2, R) \rangle \\ &= U_0(r_1, R) U_0^*(r_2, R) \langle \exp[\Psi(r_1, R) + \Psi^*(r_2, R)] \rangle, \end{aligned} \quad (2.63)$$

where $*$ denotes complex conjugate and notation $\langle \rangle$ denotes the ensemble average which can be calculated using the following equation:

$$\langle \exp(\Psi) \rangle = \exp \left[\langle \Psi \rangle + \frac{1}{2} \left(\langle \Psi^2 \rangle - \langle \Psi \rangle^2 \right) \right]. \quad (2.64)$$

These ensemble averages can be expressed as linear combinations of integrals designated by $E_1(0, 0)$, $E_2(r_1, r_2)$, and $E_3(r_1, r_2)$ [16]. In particular,

$$\begin{aligned} \langle \exp [\Psi (r, R)] \rangle &= \langle \exp [\Psi_1 (r, R) + \Psi_2 (r, R)] \rangle \\ &= \exp [E_1 (0, 0)], \end{aligned} \quad (2.65)$$

$$\begin{aligned} \langle \exp [\Psi (r_1, R) + \Psi^* (r_2, R)] \rangle &= \langle \exp [\Psi_1 (r_1, R) + \Psi_2 (r_1, R) + \Psi_1^* (r_2, R) \\ &\quad + \Psi_2^* (r_2, R)] \rangle \\ &= \exp [2E_1 (0, 0) + E_2 (r_1, r_2)] \end{aligned} \quad (2.66)$$

and

$$\begin{aligned} &\langle \exp [\Psi (r_1, R) + \Psi^* (r_2, R) + \Psi (r_3, R) + \Psi^* (r_4, R)] \rangle \\ &= \langle \exp [\Psi (r_1, R) + \Psi_2 (r_1, R) + \Psi_1^* (r_2, R) + \Psi_2^* (r_2, R) + \Psi_1 (r_3, R) \\ &\quad + \Psi_2 (r_3, R) + \Psi_1^* (r_4, R) + \Psi_2^* (r_4, R)] \rangle \\ &= \exp [4E_1 (0, 0) + E_2 (r_1, r_2) + E_2 (r_1, r_4) + E_2 (r_3, r_2) + E_2 (r_3, r_4) \\ &\quad + E_3 (r_1, r_3) + E_3^* (r_2, r_4)]. \end{aligned} \quad (2.67)$$

Assuming a statistically homogeneous and isotropic random medium, $E_1 (0, 0)$, $E_2 (r_1, r_2)$ and $E_3 (r_1, r_2)$ in Eqs. (2.65), (2.66) and (2.67) are given as [29]

$$\begin{aligned} E_1 (0, 0) &= \langle \Psi_2 (r, R) \rangle + 1/2 \langle \Psi_1^2 (r, R) \rangle \\ &= -2\pi^2 k^2 \sec (\theta) \int_{h_0}^H \int_0^\infty \kappa \Phi_n (h, \kappa) d\kappa dh, \end{aligned} \quad (2.68)$$

$$\begin{aligned} E_2 (r_1, r_2) &= \langle \Psi_1 (r_1, R) \Psi_1^* (r_2, R) \rangle \\ &= 4\pi^2 k^2 \sec (\theta) \int_{h_0}^H \int_0^\infty \kappa \Phi_n (h, \kappa) \\ &\quad \cdot \exp (-\Lambda L \kappa^2 \xi^2 / k) \\ &\quad \cdot J_0 [\kappa | (1 - \bar{\Theta} \xi) \rho - 2i \Lambda \xi r |] d\kappa dh \end{aligned} \quad (2.69)$$

and

$$\begin{aligned} E_3 (r_1, r_2) &= \langle \Psi_1 (r_1, R) \Psi_1 (r_2, R) \rangle \\ &= -4\pi^2 k^2 \sec (\theta) \int_{h_0}^H \int_0^\infty \kappa \Phi_n (h, \kappa) \\ &\quad \cdot \exp (-\Lambda R \kappa^2 \xi^2 / k) J_0 [(1 - \bar{\Theta} \xi - i \Lambda \xi) \kappa \rho] \end{aligned}$$

$$\cdot \exp \left[-\frac{i\kappa^2 R}{k} \xi (1 - \bar{\Theta} \xi) \right] d\kappa dh. \quad (2.70)$$

In the above equations, $i^2 = -1$, $\rho = r_1 - r_2$, and $r = 1/2 (r_1 + r_2)$, $J_0(x)$ is the Bessel function, and $\Phi_n(h, \kappa)$ is the power spectrum of refractive index fluctuations commonly defined by classical Kolmogorov spectrum. The parameter ξ is the normalized distance variable and is given as $\xi = 1 - (h - h_0) / (H - h_0)$ for the uplink propagation and $\xi = (h - h_0) / (H - h_0)$ for downlink propagation. The parameter $\bar{\Theta} = 1 - \Theta$ is the complementary beam parameter. The conventional Rytov approximation is then used to calculate the mean intensity at the receiver and is given by

$$\langle I(r, R) \rangle = I_0(r, R) \exp [2E_1(0, 0) + E_2(r, r)], \quad (2.71)$$

where I_0 is the intensity profile at the receiver without atmospheric turbulence and given by Eq. (2.58). Assuming the mean intensity to be approximated by Gaussian spatial profile, the above equation can be expressed as [30]

$$\langle I(r, R) \rangle = \frac{W_0^2}{W_e^2} \exp \left(\frac{-2r^2}{W_e^2} \right) [\text{W/m}^2], \quad (2.72)$$

where W_e is the effective spot size of the Gaussian beam in the presence of the optical turbulence. The effective spot size W_e for an uplink ground-to-satellite link is given by [16, 21]

$$W_e = W (1 + T_{ss})^{1/2}, \quad (2.73)$$

where

$$\begin{aligned} T_{ss} &= -2E_1(0, 0) - E_2(0, 0) \\ &= 4\pi^2 k^2 \sec(\theta) \int_{h_0}^H \int_0^\infty \kappa \Phi_n(h, \kappa) \\ &\quad \cdot \left\{ 1 - \exp \left[-\frac{\Lambda R \kappa^2}{k} \left(1 - \frac{h - h_0}{H - h_0} \right) \right] \right\} d\kappa dh. \end{aligned} \quad (2.74)$$

For downlink path, T_{ss} is given by

$$T_{ss} = 4\pi^2 k^2 \sec(\theta) \int_{h_0}^H \int_0^\infty \kappa \Phi_n(h, \kappa)$$

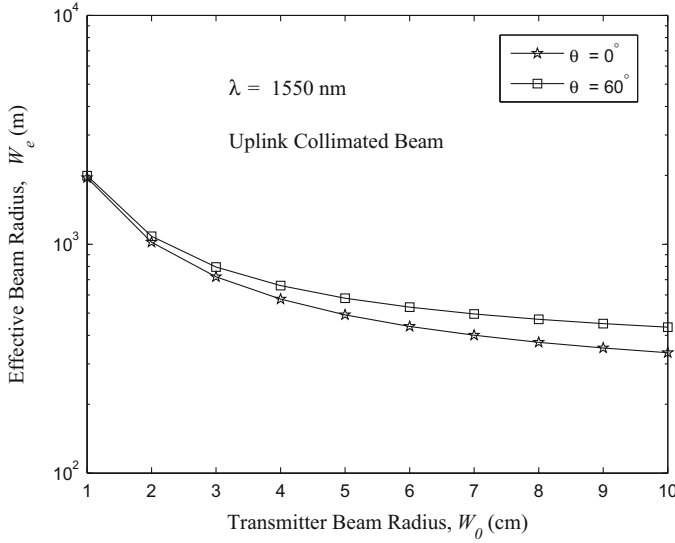


Fig. 2.17 Effective beam radius at the receiver (in m) as a function of transmitter beam radius (in cm) for various zenith angles

$$\cdot \left\{ 1 - \exp \left[-\frac{\Lambda R \kappa^2}{k} \left(\frac{h - h_0}{H - h_0} \right) \right] \right\} d\kappa dh. \quad (2.75)$$

It is seen from Eqs. (2.74) and (2.75) that for both uplink and downlink, turbulence-induced mean irradiance is completely determined by the beam spot size at the receiver. Figure 2.17 shows the effective beam radius/spot size at the receiver as a function of transmitter beam radius for ground-to-satellite uplink. It is clear that effective beam size at the receiver decreases rapidly up to almost 4 cm. For larger transmitter beam size, i.e., $W_0 > 4$ cm, the effective beam size decreases further, but the decrease is not very much. For downlink paths, the effective spot size in the presence of turbulence is essentially the same as the diffraction spot size W . This is due to the fact that level of turbulence at the higher altitude is less than that at the ground level.

2.1.3.2 Modified Rytov Approximation

The conventional Rytov method discussed above is generally limited to weak fluctuation conditions. So a modified version of Rytov approximation has been developed which is applicable under weak to strong atmospheric fluctuations. For this, the following basic assumptions are made:

- (i) The received irradiance fluctuations can be modeled as a modulation process in which the small-scale (diffracting) and large-scale (refracting) fluctuations are multiplicative.

- (ii) The small- and large-scale processes are statistically independent.
- (iii) The Rytov method for optical scintillation is valid even in the saturation regime by using spatial frequency filters to account for the loss of spatial coherence of the optical wave in strong fluctuation conditions.

Therefore, the normalized irradiance is written as $I = XY$, where X and Y are the statistically independent random quantities arising from large-scale and small-scale turbulent eddies. It is assumed that X and Y have unity mean, i.e., $\langle X \rangle = \langle Y \rangle = 1$. Therefore, in this case, $\langle I \rangle = 1$ and the second moment of irradiance $\langle I^2 \rangle$ is given by

$$\begin{aligned} \langle I^2 \rangle &= \langle X^2 \rangle \langle Y^2 \rangle \\ &= (1 + \sigma_x^2) (1 + \sigma_y^2). \end{aligned} \quad (2.76)$$

where σ_x^2 and σ_y^2 are the normalized variance of the large- and small-scale irradiance fluctuations, respectively. Further, the scintillation index is given by

$$\begin{aligned} \sigma_I^2 &= \frac{\langle I^2 \rangle}{\langle I \rangle^2} - 1 \\ &= (1 + \sigma_x^2) (1 + \sigma_y^2) - 1 \\ &= \sigma_x^2 + \sigma_y^2 + \sigma_x^2 \sigma_y^2 \end{aligned} \quad (2.77)$$

Therefore, the normalized variance σ_x^2 and σ_y^2 can be written in terms of log-irradiance variance,

$$\begin{aligned} \sigma_x^2 &= \exp(\sigma_{\ln x}^2) - 1 \\ \sigma_y^2 &= \exp(\sigma_{\ln y}^2) - 1, \end{aligned} \quad (2.78)$$

where $\sigma_{\ln x}^2$ and $\sigma_{\ln y}^2$ are the large- and small-scale log-irradiance variances, respectively. Hence, total scintillation index will be

$$\sigma_I^2 = \exp(\sigma_{\ln I}^2) - 1 = \exp(\sigma_{\ln x}^2 + \sigma_{\ln y}^2) - 1. \quad (2.79)$$

In case of weak fluctuations, the scintillation index in Eq. (2.79) reduces to the limiting form [16, 31]

$$\sigma_I^2 \approx \sigma_{\ln I}^2 \approx \sigma_{\ln x}^2 + \sigma_{\ln y}^2. \quad (2.80)$$

2.2 Atmospheric Turbulent Channel Model

Beam propagation in the atmosphere can be described by the following wave equation [32–35]

$$\nabla^2 U + k^2 n^2(r) U = 0, \quad (2.81)$$

where $\text{emph}U$ and k represent electric field and wave number ($2\pi/\lambda$), respectively, ∇^2 is the Laplacian operator given as $\nabla^2 = \partial^2/\partial x^2 + \partial^2/\partial y^2 + \partial^2/\partial z^2$. The parameter n is the refractive index of medium that is generally a random function of space and is given by Eq. (2.27). When an optical beam propagates through the atmosphere, random fluctuations in air temperature and pressure produce refractive index inhomogeneities that affect the amplitude and phase of the beam. The wavefront perturbations introduced by the atmosphere can be physically described by the Kolmogorov model. The associated power spectral density for the refractive index fluctuations is defined as

$$\Phi_n(\kappa) = 0.033C_n^2\kappa^{-11/3}\frac{1}{L_0} \ll \kappa \ll \frac{1}{l_0}, \quad (2.82)$$

where κ is the scalar spatial frequency (in rad/m). The value of C_n^2 is essentially fixed for horizontal propagation over reasonable distance. Typically, its value ranges from $10^{-17} \text{ m}^{-2/3}$ (for weak turbulence) up to $10^{-13} \text{ m}^{-2/3}$ (for strong turbulence). However, for vertical or slant propagation, the C_n^2 varies as a function of height above the ground. In that case, the average value over the entire propagation path is taken. It is dependent on various parameters like temperature, atmospheric pressure, altitude, humidity, wind speed, etc. Therefore, it is convenient to model the strength of turbulence in the atmosphere based on some empirical scintillation data.

The measured data for C_n^2 can be classified into boundary layer and free space depending upon the height above the ground. The boundary layer is the region close to the Earth surface having large temperature and pressure fluctuations resulting in large convective instabilities. This region extends from hundreds of meters to about 2 km above the surface. Further, large variations in the value of C_n^2 are observed depending upon the location, time of the day, wind speed, and solar heating. A good example of boundary layer C_n^2 measurement shows diurnal variations with peak at afternoon, dips during neutral duration close to sunrise and sunset, and almost constant value at night. The date time measurement of structure constant profile as a function of altitude shows $(-4/3)$ dependence of C_n^2 on altitude. On the other hand, the free atmosphere layer involves the altitude in the vicinity of the tropopause (15–17 km) and higher altitudes. The value of C_n^2 at higher altitudes is very small. Based on these measurements, various empirical models of C_n^2 have been proposed [36, 37]. All these models describe the strength of the atmospheric turbulence with respect to the altitude. As it is not easy to capture all the variations of C_n^2 , none of the models describe the characteristic of turbulence with sufficient accuracy. The structure parameter constant C_n^2 evaluated from Fried model is shown in Fig. 2.18. This model is one of the oldest models and is given as [2]

$$C_n^2(h) = K_0 h^{-1/3} \exp\left(-\frac{h}{h_0}\right), \quad (2.83)$$

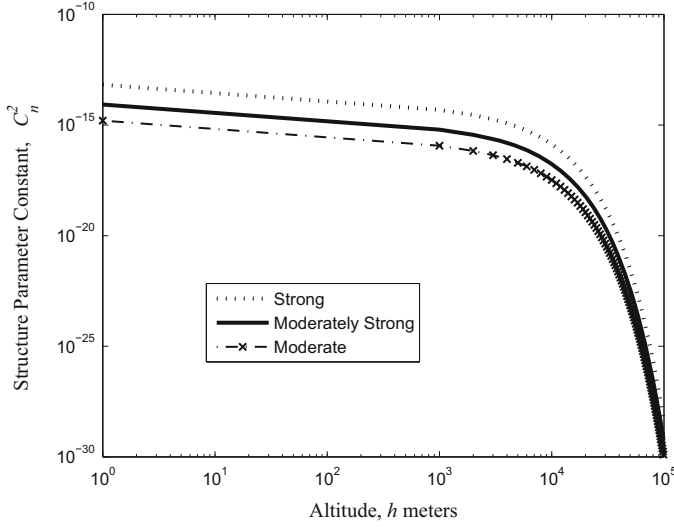


Fig. 2.18 Variations of atmospheric structure constant with altitude for the Fried model

where K_0 is the turbulence strength parameter in units of $m^{-1/3}$ and h the altitude in meters. Typical values of K_0 for strong, moderately strong, and moderate turbulence are

$$K_0 = \begin{cases} 6.7 \times 10^{-14} & \text{Strong} \\ 8.5 \times 10^{-15} & \text{Moderately strong} \\ 1.6 \times 10^{-15} & \text{Moderate} \end{cases} \quad (2.84)$$

The Hufnagel-Valley Boundary (HVB) model [20] based on various empirical scintillation data of the atmosphere is given below

$$C_n^2(h) = 0.00594 \left[\left(\frac{V}{27} \right)^2 (10^{-5}h)^{10} \exp(-h/1000) + 2.7 \times 10^{-16} \exp\left(-\frac{h}{1500}\right) + A \exp\left(-\frac{h}{100}\right) \right] m^{-2/3}, \quad (2.85)$$

where V^2 is the mean square value of the wind speed in m/s, h is the altitude in meters, and A is a parameter whose value can be adjusted to fit various site conditions. The parameter A is given as

$$A = 1.29 \times 10^{-12} r_0^{-5/3} \lambda^2 - 1.61 \times 10^{-13} \theta_0^{-5/3} \lambda^2 - 3.89 \times 10^{-15}. \quad (2.86)$$

In the above equation, θ_0 is the isoplanatic angle [38] (angular distance over which the atmospheric turbulence is essentially unchanged) and r_0 the atmospheric

coherence length as defined earlier. For $\theta_0 = 7 \mu\text{rad}$ and $r_0 = 5 \text{ cm}$ at $\lambda = 1550 \text{ nm}$, calculated value of A is $3.1 \times 10^{-13} \text{ m}^{-2/3}$. These values correspond to HVB 5/7 model. The root mean square wind velocity V between altitude of 5 and 20 km above the sea level is given by

$$V = \left[\frac{1}{15} \int_5^{20} v^2(h) dh \right]^{1/2}. \quad (2.87)$$

Another very simple model given by Hufnagel and Stanley (HS) [2] is

$$C_n^2(h) = \begin{cases} \frac{1.5 \times 10^{-13}}{h} & h \leq 20 \text{ km} \\ 0 & h > 20 \text{ km} \end{cases}, \quad (2.88)$$

where h is the altitude above the ground and is assumed to be less than 2500 m. A new model based on empirical and experimental observations of $C_n^2(h)$ is CLEAR 1 model [20]. This model typically describes the nighttime profile of refractive index structure constant for altitude $1.23 \text{ km} < h < 30 \text{ km}$. It is obtained by averaging and statistically interpolating the observations obtained over a large number of meteorological conditions. It is given as [39]

$$C_n^2(h) = \begin{cases} 10^{-17.025-4.3507h+0.814h^2} & \text{for } 1.23 < h \leq 2.13 \text{ km} \\ 10^{-16.2897+0.0335h-0.0134h^2} & \text{for } 2.13 < h \leq 10.34 \text{ km} \\ 10^{-17.0577-0.0449h-0.00051h^2+0.6181\exp(-0.5(h-15.5617)/12.0173)} & \text{for } 10.34 < h \leq 30 \text{ km} \end{cases} \quad (2.89)$$

where h is the altitude expressed in km. The refractive index structure constant, $C_n^2(h)$, is likely to be zero above 30 km. Another $C_n^2(h)$ model is submarine laser communication (SLC) [16] that was developed in Maui, Hawaii. The daytime profile of $C_n^2(h)$ is given by

$$C_n^2(h) = \begin{cases} 8.4 \times 10^{-15} & h \leq 18.5 \text{ m} \\ \frac{(3.13 \times 10^{-13})}{h} & 18.5 < h \leq 240 \text{ m} \\ 1.3 \times 10^{-15} & 240 < h \leq 880 \text{ m} \\ \frac{8.87 \times 10^{-7}}{h^3} & 880 < h \leq 7200 \text{ m} \\ \frac{2 \times 10^{-16}}{\sqrt{h}} & 7200 < h \leq 20,000 \text{ m} \end{cases}. \quad (2.90)$$

A comparison of four models, i.e., HVB, HS, CLEAR 1, and SLC models, of atmospheric profile of the refractive index structure constant is shown in Fig. 2.19. Table 2.5 gives the description of various turbulence profile models used in FSO communication systems.

It is observed from Fig. 2.18 that Fried model is applicable for short-range propagation path for various strengths of atmospheric turbulence. HS, CLEAR 1, and SLC models are applicable for long-range propagation, but they cannot provide

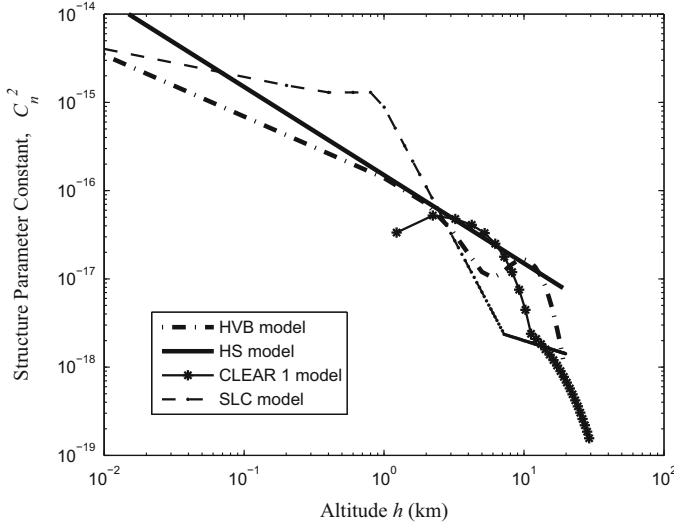


Fig. 2.19 Comparison of HVB, HS, CLEAR 1, and SLC models for atmospheric structure parameter constant

fairly good information about different site conditions. Hence, a very careful choice of $C_n^2(h)$ has to be made for determining the correct strength of turbulence in the atmosphere. The HVB model of atmospheric turbulence is most widely used for ground-to-satellite communication as it agrees fairly well with the measured values. This model includes part of upper atmosphere from 3 to 24 km, and it applies for both daytime and nighttime measurements. Further, it allows the adjustment of two parameters, i.e., coherence length, r_0 , and iso-planatic angle, θ_0 in the model to simulate various site conditions.

The $C_n^2(h)$ profile as a function of height above the ground for various rms wind speeds V is shown in Fig. 2.20. It can be seen from this figure that there is a little effect of V up to a height of 1 km. Beyond this, wind speed governs the HVB profile behavior which shows a peak in the vicinity of 10 km. Therefore, for long-distance communication, wind speed effectively determines the fluctuations in irradiance of the received signal.

It can be seen that over the range $l_0 \leq r_0 \leq L_0$, variance of log-irradiance (or Rytov variance) can be written in terms of refractive index structure parameter, C_n^2 as

$$\sigma_R^2 \approx 2.24k^{7/6} (\sec(\theta))^{11/6} \int_{h_0}^H C_n^2(h) h^{5/6} dh. \quad (2.91)$$

It is observed from Eq. (2.91) that log-irradiance variance increases with the increase in the value of C_n^2 , zenith angle θ , or path length H . Substituting Eq. (2.85) into Eq. (2.91) gives the variance of log-irradiance σ_R^2 as

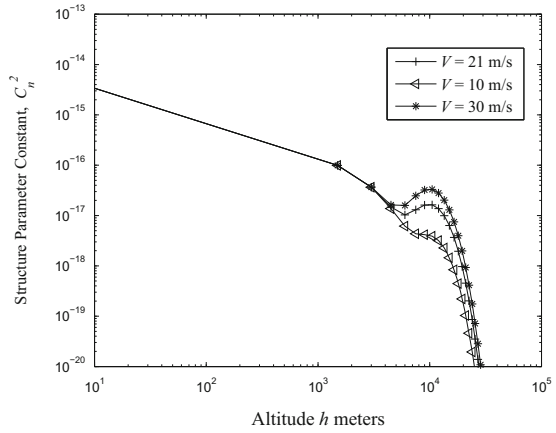
Table 2.5 Turbulence profile models for C_n^2

Models	Range	Comments
PAMELA model [40]	Long (few tens of kms)	<ul style="list-style-type: none"> – Robust model for different terrains and weather type – Sensitive to wind speed – Does not perform well over marine/overseas environment
NSLOT model[41]	Long (few tens of kms)	<ul style="list-style-type: none"> – More accurate model for marine propagation – Surface roughness is “hardwired” in this model – Temperature inversion, i.e., ($T_{air} - T_{sur} > 0$), is problematic
Fried model [42]	Short (in meters)	<ul style="list-style-type: none"> – Support weak, strong, and moderate turbulence
Hufnagel and Stanley Model [43]	Long (few tens of kms)	<ul style="list-style-type: none"> – C_n^2 is proportional to h^{-1} – Not suitable for various site conditions
Hufnagel valley model [44, 45]	Long (few tens of kms)	<ul style="list-style-type: none"> – Most popular model as it allows easy variation of daytime and nighttime profile by varying various site parameters like wind speed, iso-planatic angle, and altitude – Best suited for ground-to-satellite uplink – HV 5/7 is a generally used to describe C_n^2 profile during daytime. HV5/7 yields a coherence length of 5 cm and isoplanatic angle of 7 μrad at 0.5 μm wavelength
Gurvich model [46]	Long (few tens of kms)	<ul style="list-style-type: none"> – Covers all regimes of turbulence from weak, moderate to strong – C_n^2 dependance on altitude, h, follows power law i.e., $C_n^2 \propto h^{-n}$ where n could be 4/3, 2/3, or 0 for unstable, neutral, or stable atmospheric conditions, respectively
Von Karman-Tatarski model [47, 48]	Medium (few kms)	<ul style="list-style-type: none"> – Make use of phase perturbations of laser beam to estimate inner and outer scale of turbulence – Sensitive to change in temperature difference
Greenwood model [49]	Long (few tens of kms)	<ul style="list-style-type: none"> – Nighttime turbulence model for astronomical imaging from mountain top sites
Submarine laser communication (SLC) [50] model	Long (few tens of kms)	<ul style="list-style-type: none"> – Well suited for daytime turbulence profile at inland sites – Developed for AMOS observatory in Maui, Hawaii
Clear 1 [20]	Long (few tens of kms)	<ul style="list-style-type: none"> – Well suited for nighttime turbulent profile – Averages and statistically interpolate radiosonde observation measurements obtained from large number of meteorological conditions

(continued)

Table 2.5 (continued)

Models	Range	Comments
Aeronomy laboratory model (ALM) [51]	Long (few tens of kms)	<ul style="list-style-type: none"> – Shows good agreement with radar measurements – Based on relationship proposed by Tatarski [48] and works well with radiosonde data
AFRL radiosonde model [52]	Long (few tens of kms)	<ul style="list-style-type: none"> – Similar to ALM but with simpler construction and more accurate results as two separate models are used for troposphere and stratosphere – Daytime measurements could give erroneous results due to solar heating of thermosonde probes

Fig. 2.20 $C_n^2(h)$ profile as a function of altitude

$$\sigma_R^2 \approx \left[7.41 \times 10^{-2} \left(\frac{V}{27} \right)^2 + 4.45 \times 10^{-3} \right] \lambda^{-7/6} (\sec(\theta))^{11/6}. \quad (2.92)$$

Variations of σ_R^2 with rms wind velocity V for different θ at $\lambda = 1064$ nm obtained from this equation are shown in Fig. 2.21. It is observed that the irradiance fluctuations increase with the increase in V and is less at lower value of θ for the same value of V . Typical value of θ lies between 0° and 60° .

2.3 Techniques for Turbulence Mitigation

In FSO communication, turbulence in the atmosphere results in irradiance fluctuations or beam wander effect of received signal, leading to an increased bit error rate (BER) in the system. Irradiance fluctuations (or scintillation) and beam wander effect induce deep signal fades when an optical signal propagates through turbulent

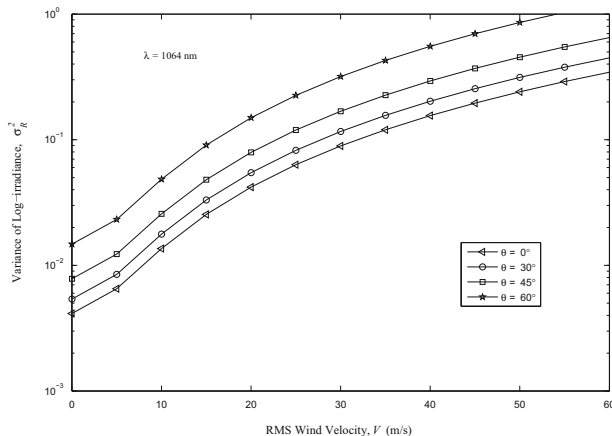
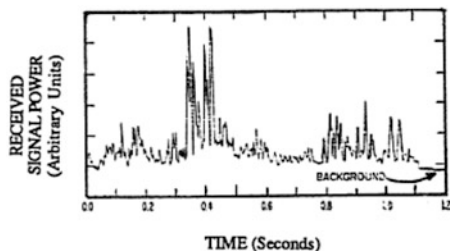


Fig. 2.21 Log-irradiance variance as a function of rms wind velocity V for zenith angle $\theta = 0^\circ, 30^\circ, 40^\circ$ and 60°

Fig. 2.22 Power fluctuations for small detector placed 145 km from the transmitter [54]



atmosphere. This deep signal fade lasts for $1\text{--}100\ \mu\text{s}$ [53]. If a link is operating at say, 1 Gbps, this could result in the loss of up to 10^5 consecutive bits. This introduces the burst errors that effectively degrade the performance of the FSO link and reduce the system availability. Therefore, some mitigation technique has to be employed in order to avoid this huge data loss due to turbulence-induced irradiance fluctuations and beam wander. Various techniques to mitigate the effect of turbulence-induced signal fading are discussed below.

2.3.1 Aperture Averaging

If the size of receiver aperture is considerably smaller than the beam diameter, then the received beam will experience lots of intensity fluctuations due to turbulence in the atmosphere. Typical power fluctuations recorded by the detector of small area are shown in Fig. 2.22.

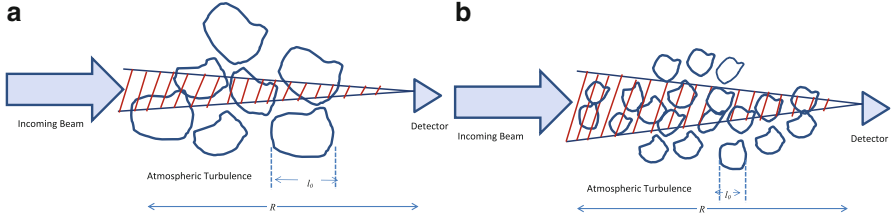


Fig. 2.23 Scattered optical signal from turbulent cells within acceptance cone (a) geometrical optics hold good if cone width is less than the cell dimension and (b) diffraction effect becomes important if cone width include many turbulent cells

The fluctuations in the received power can be explained with the help of illustration shown in Fig. 2.23. The atmosphere will provide an acceptance angle for the receiver assuming detector at the receiver to be omnidirectional. The scattered optical signal from turbulent cells within the acceptance cone will contribute to the received signal power. These turbulent cells form a diffracting aperture with average size l , and therefore, the angle formed by the acceptance cone is given by $\theta \cong \lambda/l$. The largest acceptance cone will be for smallest eddy size (inner scale of turbulent eddy), l_0 , so that

$$\theta_{\max} \cong \frac{\lambda}{l_0}. \quad (2.93)$$

The maximum width of the cone is $R\theta_{\max}$, and as long as this width is less than inner scale of turbulent eddy, l_0 , geometrical optics produce good results. Therefore, geometrical optics is valid when [55]

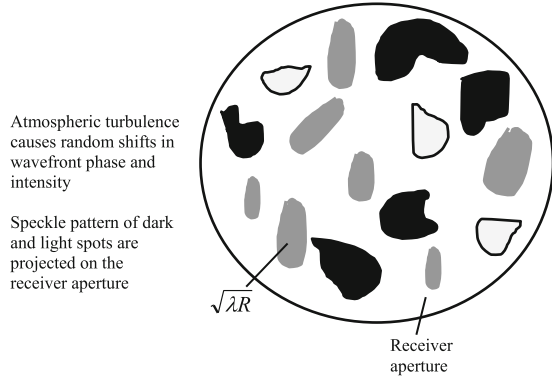
$$\theta_{\max} R = \frac{\lambda}{l_0} \cdot R < l_0, \quad (2.94)$$

or

$$\sqrt{\lambda R} < l_0. \quad (2.95)$$

However, if $\sqrt{\lambda R} \geq l_0$, then the acceptance cone may contain many smaller cells, and the received power will experience more power fluctuations as long as receiver aperture is less than beam diameter. If the diameter of the receiver aperture is made larger, receiver will average out the fluctuations over the aperture, and the irradiance fluctuations will be less than that of point receiver. This effect can be very well understood with the help of Fig. 2.24. The figure shows receiver aperture with dark and light speckles of size $\sqrt{\lambda R}$. If there is a point receiver, it will collect only one speckle that will fluctuate randomly leading to degradation in system performance. However, if the size of receiver aperture is increased, it will enhance the received power level and average out fluctuations caused by these speckles leading to

Fig. 2.24 Speckle spot formation on the receiver plane [56]



improved BER performance. The parameter that is usually used to quantify the reduction in power fluctuations by aperture averaging is called aperture averaging factor, A_f [57]. It is defined as the ratio of normalized variance of the irradiance fluctuations from a receiver with aperture diameter D_R to that from a receiver with a point aperture, i.e.,

$$A_f = \frac{\sigma_I^2(D_R)}{\sigma_I^2(0)}, \quad (2.96)$$

where $\sigma_I^2(D_R)$ and $\sigma_I^2(0)$ are the scintillation indices for receiver with aperture diameter D_R and point receiver ($D_R \approx 0$), respectively. In [57] the factor A_f is approximated, and it is given by

$$A_f \simeq \left[1 + A_0 \left(\frac{D_R^2}{\lambda h_0 \sec(\theta)} \right)^{7/6} \right]^{-1}, \quad (2.97)$$

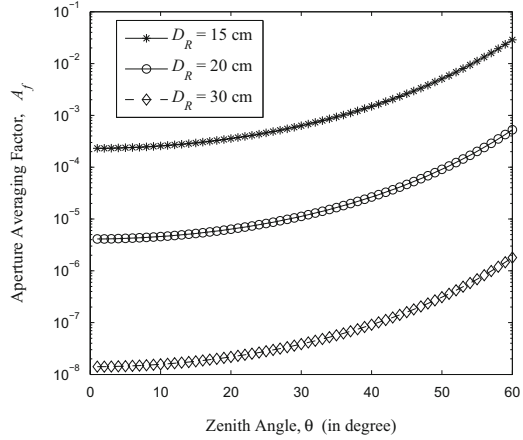
where $A_0 \approx 1.1$ and h_0 the atmospheric turbulence aperture averaging scale height. It is given as [57]

$$h_0 = \left[\frac{\int_0^H C_n^2(h) h^2 dh}{\int_0^H C_n^2(h) h^{5/6} dh} \right]^{6/7}. \quad (2.98)$$

This relation takes into account the slant path propagation through the atmosphere and permits the modeling of the atmospheric refractive index function. Figure 2.25 shows the variations of aperture averaging factor for different aperture diameters using HVB 5/7 model with $V = 21$ m/s. It is evident from this figure that there is an improvement in the aperture averaging factor implying decrease in

Fig. 2.25 Variations of aperture averaging factor with zenith angle θ for various values of receiver aperture diameter

$D_R = 15, 20$ and 30 cm using HVB 5/7 model



the value of A_f with the increase in the receiver aperture diameter D_R . Further, the aperture averaging factor degrades with the increase in zenith angle.

2.3.2 Spatial Diversity

It is not always possible to increase the receiver aperture diameter beyond a certain level as it will lead to increase in background noise. Hence, increasing receiver aperture may not be an optimum solution. To achieve the same level of performance as an aperture integrator receiver, the single large aperture is replaced by array of small apertures (either at the transmitter or at the receiver) that are sufficiently separated from each other. The separation between the multiple apertures should be greater than the coherence length, r_0 , of the atmosphere so that multiple beams are independent and at least uncorrelated. This technique of employing multiple apertures either at the transmitter (also called transmit diversity) or at the receiver (also called receive diversity) or at both sides (also called multiple input multiple output – MIMO) to mitigate the effect of turbulence is known as spatial diversity [58] as shown in Fig. 2.26. If a single laser beam is used for transmission through the atmosphere, turbulence in the atmosphere will cause the beam to split up into various small beam segments. These segments will then independently move around due to local changes in the refractive index of the atmosphere. At the receiver, various segments will either combine inphase or out of phase with respect to each other. Inphase events will cause surge in the power, whereas out-of-phase events will cause severe signal fades, and these lead to random fluctuations in the power at the receiver. If instead of single beam, multiple independent, and uncorrelated spatially diverse beams are used for transmission, then any overlapping of beams at the receiver will result in addition of power from different beams. Furthermore, the probability of deep fades and surges will be reduced significantly.

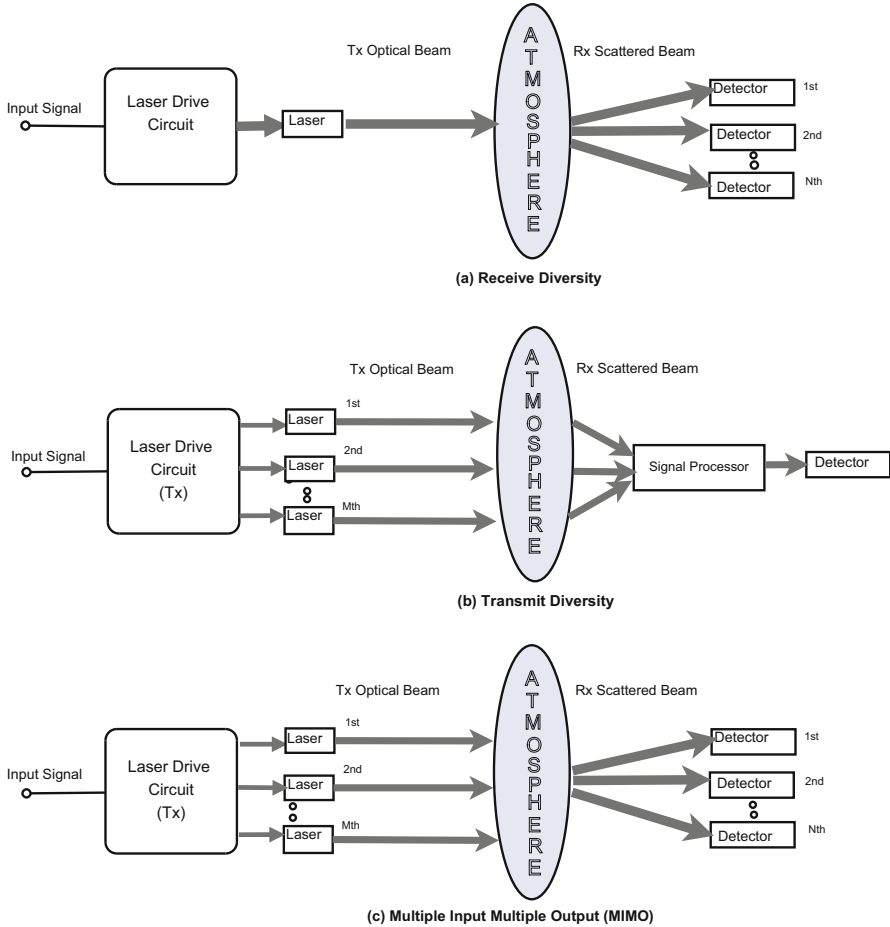


Fig. 2.26 Concept of (a) receive diversity, (b) transmit diversity and (c) multiple input multiple output (MIMO) techniques

Besides mitigating irradiance fluctuations due to turbulence, it also helps the FSO system designer to limit the transmitter power within allowable safe laser power limits. To determine the improvement in the performance with multiple apertures to that of single large aperture, let us take the case of array of N statistically independent detectors. In this case, the summed output is given by

$$I_r = \eta \sum_{j=1}^N (I_{s,j} + I_{n,j}), \quad (2.99)$$

where η is the optical to electrical conversion efficiency and $I_{s,j}$ and $I_{n,j}$ are signal and noise currents corresponding to j^{th} receiver, respectively. For simplicity, it is

assumed that mean and variance of signal and noise currents in all receivers are the same. With this assumption, the mean and the variance of the total received current I_r are given as

$$\langle I_r \rangle = N \langle I_{s,1} \rangle, \quad \sigma_{I_r}^2 = N \left[\langle I_{s,1}^2 \rangle - \langle I_{s,1} \rangle^2 + \langle I_{n,1}^2 \rangle \right] = N (\sigma_{s,1}^2 + \sigma_{n,1}^2). \quad (2.100)$$

Therefore, the mean rms SNR is given by

$$\langle SNR_N \rangle = \frac{N \langle I_{s,1} \rangle}{\sqrt{N (\sigma_{s,1}^2 + \sigma_{n,1}^2)}} = \sqrt{N} \langle SNR_1 \rangle, \quad (2.101)$$

where $\langle SNR_1 \rangle$ is the mean SNR of a single detector receiver. The above equation shows that the output SNR from N -independent detectors can improve the system performance by a factor of \sqrt{N} . Likewise, the effective normalized irradiance variance (scintillation index) is reduced by N i.e., [16]

$$\sigma_{I,N}^2 = \frac{1}{N} \sigma_{I,1}^2, \quad (2.102)$$

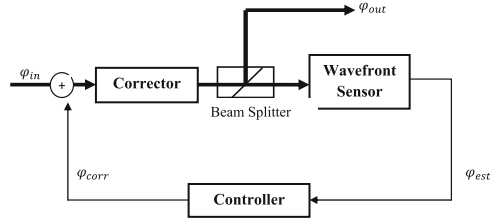
where N is the number of multiple detectors at the receivers. This is true in case of multiple transmitters (or transmit diversity) as well wherein multiple independent and uncorrelated beams are transmitted toward the receiver. The use of multiple beams significantly reduces the effect of turbulence-induced scintillation.

The number of detectors or the number of transmit beams required to achieve a given BER depends upon the strength of atmospheric turbulence. In principle, the received irradiance statistics is improved with the increase in the number of transmit or received antennae. The practical considerations, such as system complexity, cost, efficiency of transmit laser power, modulation timing accuracy, and the availability of space, will however limit the order of diversity to less than ten.

2.3.3 Adaptive Optics

Adaptive optics is used to mitigate the effect of atmospheric turbulence and helps to deliver an undistorted beam through the atmosphere. Adaptive optics system is basically a closed-loop control where the beam is pre-corrected by putting the conjugate of the atmospheric turbulence before transmitting it into the atmosphere [59]. In this way, it is able to reduce the fluctuations both in space and time. An adaptive optics system consists of wavefront sensor to measure the closed-loop phase front, corrector to compensate for the phase front fluctuations, and a deformable mirror that is driven by a suitable controller. Figure 2.27 shows the conceptual block diagram of adaptive optics system. Here, the output phase front

Fig. 2.27 Block diagram of an adaptive optics system



φ_{out} of the light is measured by wavefront sensor, and an estimated phase front is constructed φ_{est} . This phase information is in turn used by the controller to drive the corrector and subtract a quantity φ_{corr} from the input phase φ_{in} in order to compensate it (refer to Fig. 2.27).

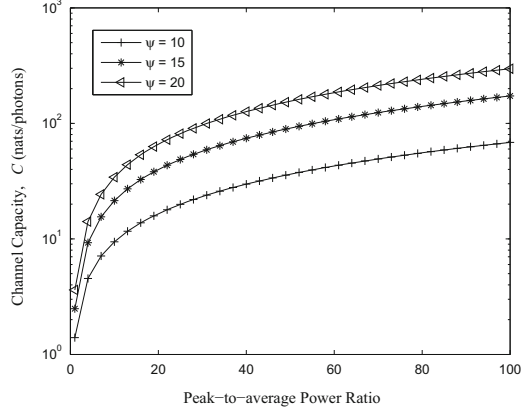
The adaptive optics is mainly used for astronomical observations. But the overall objective of adaptive optics is different for optical communication relative to astronomical observations. In astronomy, the objective is to increase the sharpness of the images, and any loss of signal energy can be made up by longer observation time. But in optical communication, the signal energy for a data bit is fixed and must be conserved for efficient communication. Therefore, an adaptive optics system has to implement an optimization system to minimize the overall FOV, i.e., to minimize the amount of background light while maximizing the amount of desired signal energy captured. This makes the design of adaptive optics system complicated and results in increased system cost.

2.3.4 Coding

Error control coding can be used in FSO link to mitigate the effect of turbulence-induced scintillation. Coding usually involves the addition of extra bits to the information which later helps the receiver in correcting the errors introduced during transmission through turbulent atmosphere. Thus, depending upon the strength of turbulence and the link range, the choice of appropriate coding techniques can significantly reduce the BER of the FSO system which can be traded for reduction in the required signal power to close the link. Besides coding, interleaving can also be used especially when the channel is bursty. The channel coding not only improves information carrying capacity but also reduces the required signal power at the receiver. The reduction in the required power level is commonly referred to as coding gain and is defined as the difference in the power levels between uncoded (in dB) and coded system (in dB) to reach the same BER level and is given as

$$\Gamma_{\text{code}} = 10 \log_{10} \left[\frac{P_{\text{req}}(\text{uncoded})}{P_{\text{req}}(\text{coded})} \right]. \quad (2.103)$$

Fig. 2.28 Channel capacity vs. peak-to-average power ratio for various ratios of signal and background photon arrival rates



According to Shannon's theorem, for a given noisy channel having capacity C and information transmission rate R_b , the probability of error can be made arbitrarily small by suitable coding technique if $R_b \leq C$. This means, theoretically it is possible to transmit information without error if the rate of transmission is below the limiting channel capacity C . The channel capacity for optical channel in the presence of background noise is given as [60]

$$C = (\log_2 e) \frac{\lambda_s}{\mathbb{P}} \left[\left(1 + \frac{1}{\psi} \right) \ln(1 + \psi) - \left(1 + \frac{\mathbb{P}}{\psi} \right) \ln \left(1 + \frac{\psi}{\mathbb{P}} \right) \right], \quad (2.104)$$

where λ_s is the rate of arrival of signal photons (in photons/sec), $\psi = \lambda_s/\lambda_B$ the detected peak signal to background photon ratio, and \mathbb{P} the peak-to-average power ratio of the signal. The variations of channel capacity C with peak-to-average power ratio \mathbb{P} from the above equation are shown in Fig. 2.28.

One of the methods commonly used to improve the channel capacity in FSO communication is to increase peak-to-average power ratio of the signal. This ratio is very much dependent upon the choice of modulation scheme. Therefore, the channel capacity can be improved by using a modulation scheme that has high peak-to-average power ratio. For this reason, M-PPM is one of the suitable modulation schemes for FSO communication system.

2.3.5 Hybrid RF/FSO

The performance of FSO communication is drastically affected by weather conditions and atmospheric turbulence. This can lead to link failures or poor BER performance of FSO system. Therefore, in order to improve the reliability and improve the availability of the link, it is wise to pair up FSO system with a more reliable RF system. Such systems are called hybrid RF/FSO and are capable

of providing high link availability even in adverse weather conditions [12]. The major cause of signal degradation in RF transmission is due to rain (as the carrier wavelength is comparable to the size of the raindrop) and in FSO communication is due to fog. So, the overall system availability can be improved by using low data rate RF link as a backup when FSO link is down. In [61], the availability of an airborne hybrid RF/FSO link is evaluated. It was observed that the FSO link provides poor availability during low cloud conditions due to the attenuation by cloud particles and temporal dispersion. However, a significant improvement was observed when a hybrid RF/FSO link was used as RF signals are immune to cloud interference. The conventional approach of hybrid RF/FSO causes inefficient use of channel bandwidth [62]. Also, a continuous switching between RF and FSO system could bring down the entire system. Therefore, a new approach as suggested in [63] gives symbol rate adaptive joint coding scheme wherein both RF and FSO subsystems are active simultaneously and save channel bandwidth. Hybrid channel coding is also capable of utilizing both the links by combining nonuniform codes and rate adaptive codes where their code rates are varied according to the channel conditions [64].

Hybrid RF/FSO link provides great application in mobile ad hoc networks (MANETs) [65]. A reconfigurable networking environment can be formed in MANETs by combination of wireless sensor network (WSN) technology and mobile robotics. The performance of this network is, however, limited by the per node throughput provided by RF-based communication. Therefore, the combination of RF and FSO provides tremendous increase in per node throughput of MANETs. The implementation of hybrid RF/FSO MANET with real-time video data routing across 100 Mbps optical link and 802.11g RF transceiver has been studied in [66].

The RF wireless network poses a strong limitation on its capacity and throughput owing to growing development in communication technology [67]. With the increasing number of users, the chances of interference from the neighboring nodes increase and that limit the performance of the RF system. FSO system on the other hand is highly directional and has very narrow beam divergence. This makes FSO system immune from any kind of interference. Therefore, the combination of FSO and RF can help in solving the capacity scarcity problem in RF networks. The through capacity of hybrid RF/FSO link is given in [68–70].

2.4 Summary

As the optical signal propagates through the atmospheric channel, it encounters variation in the intensity of the signal due to various unpredictable environmental factors like fog, rain, snow, etc. Other factors responsible for degrading the quality of the optical beam in FSO communication are absorption and scattering, beam divergence loss, free-space loss, and pointing loss. Also, turbulence in the atmosphere causes random fluctuations in the intensity and phase of the received signal. Effect of atmospheric turbulence on the Gaussian beam has been analyzed

by conventional and modified Rytov approximation. Atmospheric turbulent channel models have been discussed based on various empirical scintillation data of the atmosphere. Various statistical models to describe the irradiance statistics of the received signal due to randomly varying turbulent atmospheric channel, lognormal, negative exponential, gamma-gamma, etc. have been discussed. Various techniques to mitigate the channel fading due to atmospheric turbulence are described.

Bibliography

1. R.N. Clark, *Spectroscopy of Rocks and Minerals, and Principles of Spectroscopy & in Manual of Remote Sensing (Chapter 1)*, vol. 3. (Wiley, New York, 1999) (Disclaimer: This image is from a book chapter that was produced by personnel of the US Government therefore it cannot be copyrighted and is in the public domain)
2. R.M. Gagliardi, S. Karp, *Optical Communications*, 2nd edn. (Wiley, New York, 1995)
3. R.K. Long, Atmospheric attenuation of ruby lasers. *Proc. IEEE* **51**(5), 859–860 (1963)
4. R.M. Langer, Effects of atmospheric water vapour on near infrared transmission at sea level, in *Report on Signals Corps Contract DA-36-039-SC-723351* (J.R.M. Bege Co., Arlington, 1957)
5. A.S. Jursa, *Handbook of Geophysics and the Space Environment* (Scientific Editor, Air Force Geophysics Laboratory, Washington, DC, 1985)
6. H. Willebrand, B.S. Ghuman, *Free Space Optics: Enabling Optical Connectivity in Today's Networks* (SAMS publishing, Indianapolis, 2002)
7. M. Rouissat, A.R. Borsali, M.E. Chiak-Bled, Free space optical channel characterization and modeling with focus on algeria weather conditions. *Int. J. Comput. Netw. Inf. Secur.* **3**, 17–23 (2012)
8. H.C. Van de Hulst, *Light Scattering by Small Particles* (Dover publications, Inc., New York, 1981)
9. P. Kruse, L. McGlauchlin, R. McQuistan, *Elements of Infrared Technology: Generation, Transmission and Detection* (Wiley, New York, 1962)
10. I.I. Kim, B. McArthur, E. Korevaar, Comparison of laser beam propagation at 785 nm and 1550 nm in fog and haze for optical wireless communications. *Proc. SPIE* **4214**, 26–37 (2001)
11. M.A. Naboulsi, H. Sizun, F. de Fornel, Fog attenuation prediction for optical and infrared waves. *J. SPIE Opt. Eng.* **43**, 319–329 (2004)
12. I.I. Kim, E. Korevaar, Availability of free space optics (FSO) and hybrid FSO/RF systems. Lightpointe technical report. [Weblink: <http://www.opticalaccess.com>]
13. Z. Ghassemlooy, W.O. Popoola, Terrestrial free-space optical communications, in *Mobile and Wireless Communications Network Layer and Circuit Level Design*, ed. by S.A. Fares, F. Adachi (InTech, 2010), doi:10.5772/7698. [Weblink: <http://www.intechopen.com/books/mobile-and-wireless-communications-network-layer-and-circuit-level-design/terrestrial-free-space-optical-communications>]
14. W.K. Hocking, Measurement of turbulent energy dissipation rates in the middle atmosphere by radar techniques: a review. *Radio Sci.* **20**(6), 1403–1422 (1985)
15. R. Latteck, W. Singer, W.K. Hocking, Measurement of turbulent kinetic energy dissipation rates in the mesosphere by a 3 MHz Doppler radar. *Adv. Space Res.* **35**(11), 1905–1910 (2005)
16. L.C. Andrews, R.L. Phillips, *Laser Beam Propagation Through Random Medium*, 2nd edn. (SPIE Optical Engineering Press, Bellingham, 1988)
17. H.E. Nistazakis, T.A. Tsiftsis, G.S. Tombras, Performance analysis of free-space optical communication systems over atmospheric turbulence channels. *IET Commun.* **3**(8), 1402–1409 (2009)
18. P.J. Titterton, Power reduction and fluctuations caused by narrow laser beam motion in the far field. *Appl. Opt.* **12**(2), 423–425 (1973)

19. J.H. Churnside, R.J. Lataitis, Wander of an optical beam in the turbulent atmosphere. *Appl. Opt.* **29**(7), 926–930 (1990)
20. R.R. Beland, Propagation through atmospheric optical turbulence, in *The Infrared and Electro-Optical Systems Handbook*, vol. 2 (SPIE Optical Engineering Press, Bellingham, 1993)
21. H. Hemmati, *Near-Earth Laser Communications* (CRC Press/Taylor & Francis Group, Boca Raton, 2009)
22. L.C. Andrews, R.L. Phillips, R.J. Sasiela, R.R. Parenti, Strehl ratio and scintillation theory for uplink Gaussian-beam waves: beam wander effects. *Opt. Eng.* **45**(7), 076001-1–076001-12 (2006)
23. H.T. Yura, W.G. McKinley, Optical scintillation statistics for IR ground-to-space laser communication systems. *Appl. Opt.* **22**(21), 3353–3358 (1983)
24. J. Parikh, V.K. Jain, Study on statistical models of atmospheric channel for FSO communication link, in *Nirma University International Conference on Engineering*–(NuICONE), Ahmedabad (2011), pp. 1–7
25. H.G. Sandalidis, Performance analysis of a laser ground-station-to-satellite link with modulated gamma-distributed irradiance fluctuations. *J. Opt. Commun. Netw.* **2**(11), 938–943 (2010)
26. J. Park, E. Lee, G. Yoon, Average bit-error rate of the Alamouti scheme in gamma-gamma fading channels. *IEEE Photonics Technol. Lett.* **23**(4), 269–271 (2011)
27. M.A. Kashani, M. Uysal, M. Kavehrad, *A Novel Statistical Channel Model for Turbulence-Induced Fading in Free-Space Optical Systems*. PhD thesis, Cornell University, 2015
28. A.K. Ghatak, K. Thyagarajan, *Optical Electronics* (Cambridge University Press, Cambridge, 2006)
29. L.C. Andrews, W.B. Miller, Single-pass and double-pass propagation through complex paraxial optical systems. *J. Opt. Soc. Am.* **12**(1), 137–150 (1995)
30. L.C. Andrews, R.L. Phillips, P.T. Yu, Optical scintillation and fade statistics for a satellite-communication system. *Appl. Opt.* **34**(33), 7742–7751 (1995)
31. H. Guo, B. Luo, Y. Ren, S. Zhao, A. Dang, Influence of beam wander on uplink of ground-to-satellite laser communication and optimization for transmitter beam radius. *Opt. Lett.* **35**(12), 1977–1979 (2010)
32. N.G. Van Kampen, Stochastic differential equations. *Phys. Rep. (Sect. C Phys. Lett.)* **24**(3), 171–228 (1976)
33. B.J. Uscinski, *The Elements of Wave Propagation in Random Media* (McGraw-Hill, New York, 1977)
34. H.T. Yura, S.G. Hanson, Second-order statistics for wave propagation through complex optical systems. *J. Opt. Soc. Am. A* **6**(4), 564–575 (1989)
35. S.M. Rytov, Y.A. Kravtsov, V.I. Tatarskii, *Wave Propagation Through Random Media*, vol. 4 (Springer, Berlin, 1989)
36. N.S. Kopeika, A. Zilberman, Y. Sorani, Measured profiles of aerosols and turbulence for elevations of 2–20 km and consequences on widening of laser beams. *Proc. SPIE Opt. Pulse Beam Propag. III* **4271**(43), 43–51 (2001)
37. A. Zilberman, N.S. Kopeika, Y. Sorani, Laser beam widening as a function of elevation in the atmosphere for horizontal propagation. *Proc. SPIE Laser Weapons Tech. II* **4376**(177), 177–188 (2001)
38. G.C. Valley, Isoplanatic degradation of tilt correction and short-term imaging systems. *Appl. Opt.* **19**(4), 574–577 (1980)
39. D.H. Tofsted, S.G. O'Brien, G.T. Vaucher, An atmospheric turbulence profile model for use in army wargaming applications I. Technical report ARL-TR-3748, US Army Research Laboratory (2006)
40. E. Oh, J. Ricklin, F. Eaton, C. Gilbreath, S. Doss-Hammel, C. Moore, J. Murphy, Y. Han Oh, M. Stell, Estimating atmospheric turbulence using the PAMELA model. *Proc. SPIE Free Space Laser Commun. IV* **5550**, 256–266 (2004)
41. S. Doss-Hammel, E. Oh, J. Ricklin, F. Eaton, C. Gilbreath, D. Tsintikidis, A comparison of optical turbulence models. *Proc. SPIE Free Space Laser Commun. IV* **5550**, 236–246 (2004)

42. S. Karp, R.M. Gagliardi, S.E. Moran, L.B. Stotts, *Optical Channels: Fibers, Clouds, Water, and the Atmosphere*. (Plenum Press, New York/London, 1988)
43. R.E. Hufnagel, N.R. Stanley, Modulation transfer function associated with image transmission through turbulence media. *J. Opt. Soc. Am.* **54**(52), 52–62 (1964)
44. R.K. Tyson, Adaptive optics and ground to space laser communication. *Appl. Opt.* **35**(19), 3640–3646 (1996)
45. R.E. Hufnagel, Variation of atmospheric turbulence, in *Digest of Topical Meeting on Optical Propagation Through Turbulence* (Optical Society of America, Washington, DC, 1974), p. WA1
46. A.S. Gurvich, A.I. Kon, V.L. Mironov, S.S. Khmelevtsov, *Laser Radiation in Turbulent Atmosphere* (Nauka Press, Moscow, 1976)
47. M.R. Chatterjee, F.H.A. Mohamed, Modeling of power spectral density of modified von Karman atmospheric phase turbulence and acousto-optic chaos using scattered intensity profiles over discrete time intervals. *Proc. SPIE Laser Commun. Prop. Atmosp. Oce.* **III 9224**, 922404-1–922404-16 (2014)
48. V.I. Tatarskii, *The Effects of the Turbulent Atmosphere on Wave Propagation* (Israel Program for Scientific Translations, Jerusalem, 1971)
49. M.C. Roggermann, B.M. Welsh, *Imaging Through Turbulence* (CRC Press, Boca Raton, 1996)
50. H. Hemmati (ed.), *Near-Earth Laser Communications* (CRC Press, Boca Raton, 2009)
51. T.E. Van Zandt, K.S. Gage, J.M. Warnock, An improve model for the calculation of profiles of wind, temperature and humidity, in *Twentieth Conference on Radar Meteorology* (American Meteorological Society, Boston, 1981), pp. 129–135
52. E.M. Dewan, R.E. Good, R. Beland, J. Brown, A model for C_n^2 (optical turbulence) profiles using radiosonde data. Environmental Research Paper-PL-TR-93-2043 1121, Phillips Laboratory, Hanscom, Airforce base (1993)
53. E.J. Lee, V.W.S. Chan, Optical communications over the clear turbulent atmospheric channel using diversity: part 1. *IEEE J. Sel. Areas Commun.* **22**(9), 1896–1906 (2004)
54. A.L. Buck, Effects of the atmosphere on laser beam propagation. *Appl. Opt.* **6**(4), 703–708 (1967)
55. H. Weichel, *Laser Beam Propagation in the Atmosphere* (SPIE Press, Washington, DC, 1990)
56. S. Bloom, The physics of free space optics. Technical report, AirFiber, Inc. (2002)
57. D.L. Fried, Aperture averaging of scintillation. *J. Opt. Soc. Am.* **57**(2), 169–172 (1967)
58. T.A. Tsiftsis, H.G. Sandalidis, G.K. Karagiannidis, M. Uysal, Optical wireless links with spatial diversity over strong atmospheric turbulence channels. *IEEE Trans. Wirel. Commun.* **8**(2), 951–957 (2009)
59. S.M. Navidpour, M. Uysal, M. Kavehrad, BER performance of free-space optical transmission with spatial diversity. *IEEE Trans. Wirel. Commun.* **6**(8), 2813–2819 (2007)
60. A.D. Wyner, Capacity and error exponent for the direct detection photon channel – part 1. *IEEE Trans. Inf. Theory* **34**(6), 1449–1461 (1988)
61. W. Haiping, M. Kavehrad, Availability evaluation of ground-to-air hybrid FSO/RF links. *J. Wirel. Inf. Netw. (Springer)* **14**(1), 33–45 (2007)
62. H. Moradi, M. Falahpour, H.H. Refai, P.G. LoPresti, M. Atiquzzaman, On the capacity of hybrid FSO/RF links, in *Proceedings of IEEE, Globecom* (2010)
63. Y. Tang, M. Brandt-Pearce, S. Wilson, Adaptive coding and modulation for hybrid FSO/RF systems, in *Proceeding of IEEE, 43rd Asilomar Conference on Signal, System and Computers*, Pacific Grove (2009)
64. E. Ali, V. Sharma, P. Hossein, Hybrid channel codes for efficient FSO/RF communication systems. *IEEE Trans. Commun.* **58**(10), 2926–2938 (2010)
65. D.K. Kumar, Y.S.S.R. Murthy, G.V. Rao, Hybrid cluster based routing protocol for free-space optical mobile ad hoc networks (FSO/RF MANET), in *Proceedings of the International Conference on Frontiers of Intelligent Computing*, vol. 199 (Springer, Berlin/Heidelberg, 2013), pp. 613–620
66. J. Derenick, C. Thorne, J. Spletzer, Hybrid Free-space Optics/Radio Frequency (FSO/RF) networks for mobile robot teams, in *Multi-Robot Systems: From Swarms to Intelligent Automata*, ed. by A.C. Schultz, L.E. Parke (Springer, 2005)

67. S. Chia, M. Gasparroni, P. Brick, The next challenge for cellular networks: backhaul. Proc. IEEE Microw. Mag. **10**(5), 54–66 (2009)
68. C. Milner, S.D. Davis, Hybrid free space optical/Rf networks for tactical operations, in *Military Communications Conference (MILCOM)*, Monterey (2004)
69. A. Kashyap, M. Shayman, Routing and traffic engineering in hybrid RF/FSO networks, in *IEEE International Conference on Communications* (2005)
70. B. Liu, Z. Liu, D. Towsley, On the capacity of hybrid wireless network, in *IEEE INFOCOM'03* (2003)

<http://www.springer.com/978-81-322-3689-4>

Free Space Optical Communication

Kaushal, H.; Jain, V.K.; Kar, S.

2017, XXIX, 209 p. 111 illus., 49 illus. in color.,

Hardcover

ISBN: 978-81-322-3689-4